*Article*

# A stimulus-contingent positive feedback loop enables IFN-β dose-dependent activation of pro-inflammatory genes

Catera L Wilder[1,*,†], Diane Lefaudeux[1,‡], Raisa Mathenge[1,§], Kensei Kishimoto[1,¶], Alma Zuniga Munoz[1,#], Minh A Nguyen[1,††], Aaron S Meyer[2], Quen J Cheng[1,3] (iD) & Alexander Hoffmann[1,*] (iD)

## Abstract

Type I interferons (IFN) induce powerful antiviral and innate immune responses via the transcription factor, IFN-stimulated gene factor (ISGF3). However, in some pathological contexts, type I IFNs are responsible for exacerbating inflammation. Here, we show that a high dose of IFN-β also activates an inflammatory gene expression program in contrast to IFN-λ3, a type III IFN, which elicits only the common antiviral gene program. We show that the inflammatory gene program depends on a second, potentiated phase in ISGF3 activation. Iterating between mathematical modeling and experimental analysis, we show that the ISGF3 activation network may engage a positive feedback loop with its subunits IRF9 and STAT2. This network motif mediates stimulus-specific ISGF3 dynamics that are dependent on ligand, dose, and duration of exposure, and when engaged activates the inflammatory gene expression program. Our results reveal a previously underappreciated dynamical control of the JAK–STAT/IRF signaling network that may produce distinct biological responses and suggest that studies of type I IFN dysregulation, and in turn therapeutic remedies, may focus on feedback regulators within it.

## Introduction

Host immune defense mechanisms are coordinated by interferons (IFNs). IFNs elicit cell-intrinsic antiviral activity as well as cell-extrinsic inflammatory responses leading to activation and recruitment of diverse immune cells (Sadler & Williams, 2008; Schneider *et al*, 2014; Wadman, 2020). The different families of IFNs, type I, II, and III engage these defense mechanisms to different degrees. Type I IFNs are widely known for their antiviral activity (Ivashkiv & Donlin, 2014; McNab *et al*, 2015), but in several pathological scenarios there is evidence for a role in triggering inflammation (Makris *et al*, 2017). Type II IFN is less known for generating an antiviral state, but for an enhanced activation potential state that allows macrophages to orchestrate recruitment of diverse effector cells and initiate adaptive immune responses (Ivashkiv, 2018). Like type I, type III IFNs have a primary role inducing antiviral activity, but there is less evidence for activating inflammatory mediators (Ank *et al*, 2006, 2008; Ye *et al*, 2019).

Both type I and type III IFNs activate the same JAK–STAT/IRF signaling pathway and transcription factor, ISGF3 (Mesev *et al*, 2019; Stanifer *et al*, 2019). While type I IFNs have a broad range of effectiveness due to the ubiquitous expression of the IFNAR subunits on most cell types (de Weerd & Nguyen, 2012), type III IFNs are associated with specific tissues due to the cell type-specific expression of these cytokines and the cognate IFNλR1 receptor subunit (de Weerd & Nguyen, 2012). The human type I IFN family comprises 13 subtypes of IFN-α, IFN-β, IFN-ε, IFN-κ, and IFN-ω. Type III IFNs comprise four members, namely IFN-λ1, IFN-λ2, IFN-λ3, and IFN-λ4. Altogether, there are 21 IFNs that activate the same transcription factor. This remarkable diversity of ligands activating the same transcription factor raises the question of whether their

1 Department of Microbiology, Immunology, and Molecular Genetics, University of California, Los Angeles, CA, USA
2 Department of Bioengineering, University of California, Los Angeles, CA, USA
3 Division of Infectious Diseases, Department of Medicine, University of California, Los Angeles, CA, USA
*Corresponding author. Tel: +13107949925; E-mail: ahoffmann@ucla.edu
†Present address: Department of Bioengineering and Therapeutic Sciences, University of California, San Francisco, San Francisco, CA, USA
‡Present address: Novadiscovery S.A., Lyon, France
§Present address: Division of Rheumatology, University of California, San Francisco, San Francisco, CA, USA
¶Present address: Department of Molecular, Cell, and Cancer Biology, University of Massachusetts Chan Medical School, Worcester, MA, USA
#Present address: Department of Physiology and Biophysics, University of Southern California, Los Angeles, CA, USA
††Present address: Division of Genetics and Genomics, Department of Pediatrics, Boston Children's Hospital, Boston, MA, USA

biological roles are overlapping or distinct. Studies have shown that IFN-α subtypes share the capacity to elicit antiviral states but differ in their cytostatic effects in a manner that correlates with their affinity for the IFNAR receptor (Jaks *et al*, 2007; Schreiber & Piehler, 2015). Among the type I IFNs, IFN-β has been shown to be particularly potent due to its high binding affinity and sustained life span of the IFN-IFNAR complex (Kalie *et al*, 2008; Schreiber & Piehler, 2015). Among the members of type III IFNs, IFN-λ3 has the most potent antiviral activity (Dellgren *et al*, 2009; Bolen *et al*, 2014).

While the roles of type I and III IFNs in cell-intrinsic immunity have been well-defined, their regulation of cell-extrinsic immune functions has been less well characterized. A link between type I IFNs and inflammation has been described in various infections and may involve immune cell recruitment via the expression of monocyte-recruiting chemokines (Davidson *et al*, 2014; Channappanavar *et al*, 2016; Makris *et al*, 2017; Israelow *et al*, 2020). For type III IFNs, the evidence for initiating cell-extrinsic inflammation functions is less clear (Jordan *et al*, 2007; Galani *et al*, 2017; Hemann *et al*, 2019; Read *et al*, 2019). In clinical settings, type I IFNs have been used to treat hepatitis B and COVID-19, but its adoption as an effective therapeutic has been hampered by its adverse side effects (e.g., flu-like symptoms and fatigue) associated with inflammatory cytokines (Rijckborst & Janssen, 2010; Reder & Feng, 2014; 2021). In contrast, type III IFN treatments have limited adverse effects, comparable to that of placebo groups (2021; Feld *et al*, 2021; Jagannathan *et al*, 2021).

The differential propensity of type I and III IFNs to induce inflammation could be due to cell type-specific expression of cognate receptors, or differences in signaling responses. In neutrophils, which respond to both type I and III IFNs, a type I IFN-specific inflammatory gene expression response was reported but not characterized mechanistically (Galani *et al*, 2017). However, for lung epithelial cells, key to initiating immune responses during respiratory infections, no such information is available. Importantly, both type I and III IFNs play a role in their cellular responses, as an influenza A viral challenge in primary mouse tracheal epithelial cells deficient in either IFNAR or IFNλR1 resulted in similar gene expression programs (Crotta *et al*, 2013). Hence, there is a need to investigate whether and how IFN-type I and III induce distinct responses within the same cell type.

The molecular mechanisms of signal transduction are well understood. Upon binding their cognate receptors, type I and III IFNs activate the same kinases JAK1 and TYK2, which activate the same transcription factor, ISGF3. ISGF3 is responsible for inducing the expression of hundreds of IFN-stimulated genes (ISGs; Stark & Darnell, 2012; Schneider *et al*, 2014; Mesev *et al*, 2019). ISGF3 is a trimer composed of the active, phosphorylated forms of STAT1 and STAT2 along with IRF9. The active trimer translocates to the nucleus where it binds to the promoters of ISGs to induce gene expression. While ISGF3 is the primary transcription factor induced by type I and III IFNs, others such as GAF, MAPK/ERK, and NFκB have also been implicated as IFN-inducible (Pfeffer, 2011; Pervolaraki *et al*, 2017; Mazewski *et al*, 2020; Kishimoto *et al*, 2021). A mathematical model of the IFN signaling pathway has been established and used to investigate how signaling is affected by prior IFN exposure or conditioning (Maiwald *et al*, 2010; Kok *et al*, 2020). However, whether and how ISGF3 signaling is distinct in response

to type I and III IFN stimulation has not been quantitatively examined.

Here, we investigated whether type I IFN-β and III IFN-λ3 generate distinct gene expression responses in lung epithelial cells. We identified a type I IFN-specific gene expression program that is characterized by inflammatory response mediators. Iterating between quantitative experimentation and mathematical modeling, we investigated the mechanism and report that the dynamic control of a single transcription factor, ISGF3, allows for the distinction. A secondary, potentiated phase of ISGF3 is responsible for the inflammatory gene expression program. We show that the potentiated ISGF3 activation phase is enabled by a stimulus-contingent positive feedback loop that is engaged at high doses and sustained durations of type I IFN-β. Our results indicate that stimulus-specific dynamic control of ISGF3 elicits distinct immune gene expression responses, revealing the importance of transcription network feedback control in the JAK–STAT/IRF signaling system for healthy immunity.

## Results

### IFN-β elicits both antiviral and pro-inflammatory gene expression programs

In order to determine whether IFN-β and IFN-λ3 induce differential expression of ISGs, we produced replicate RNA-seq datasets from an extensive time course. The murine MLE-12 lung epithelial cells were stimulated with either 10 U/ml IFN-β or 100 ng/ml IFN-λ3. Concentrations were selected such that the initial activation of the IFN signaling pathway was comparable as measured by ISGF3 activity at 30 min (Fig EV1), thereby sidestepping potential differences in IFNAR and IFNLR receptor expression. RNA was isolated at 11 time points of stimulation (0, 0.5, 1, 2, 3, 4, 6, 8, 12, 24, and 36 h) and subjected to polyA+ mRNA sequencing (RNA-seq) for global transcriptome analysis. A total of 345 genes were identified as inducible (FDR-corrected *P*-value < 0.05 for IFN-β dataset; Dataset EV1). Principal component analysis (PCA) of the selected genes yielded two components that accounted for almost 90% of the variance (Fig 1A). While the transcriptomes of IFN-β and IFN-λ3 time courses remain similar at early time points (0.5 and 1 h), they diverge on the PCA plot at 2 h and are well-separated at 4 h. The number of induced genes was similar at the early and late time points, but at 4 h, IFN-β showed 2.3 times as many induced genes as IFN-λ3 (FDR-corrected *P*-value < 0.05 and log$_2$(FC) ≥ 1; Fig 1B). Interestingly, even for genes induced by both stimuli at 4 h, there was a higher magnitude of induction with IFN-β (Fig 1C). However, by 24 h many genes showed a slightly higher induction with IFN-λ3.

In order to assess the temporal dynamics at a single gene level, a heatmap was generated with each row representing expression of an individual gene (Fig 1D; Dataset EV1). The selected 345 genes were grouped into two clusters based on induction by only IFN-β (cluster 1; FDR-corrected *P*-value ≤ 0.05) or by both IFN-β and IFN-λ3 (cluster 2; FDR-corrected *P*-value ≤ 0.05). Only a small subset of 27 genes were classified as IFN-λ3 specific and were not included in further analysis (Table EV3). Cluster 1 had 188 genes that generally showed transient activation with a peak at around 4 h of IFN-β stimulation. The 157 genes in cluster 2 also showed transient induction in response to IFN-β but were also induced in response to IFN-λ3
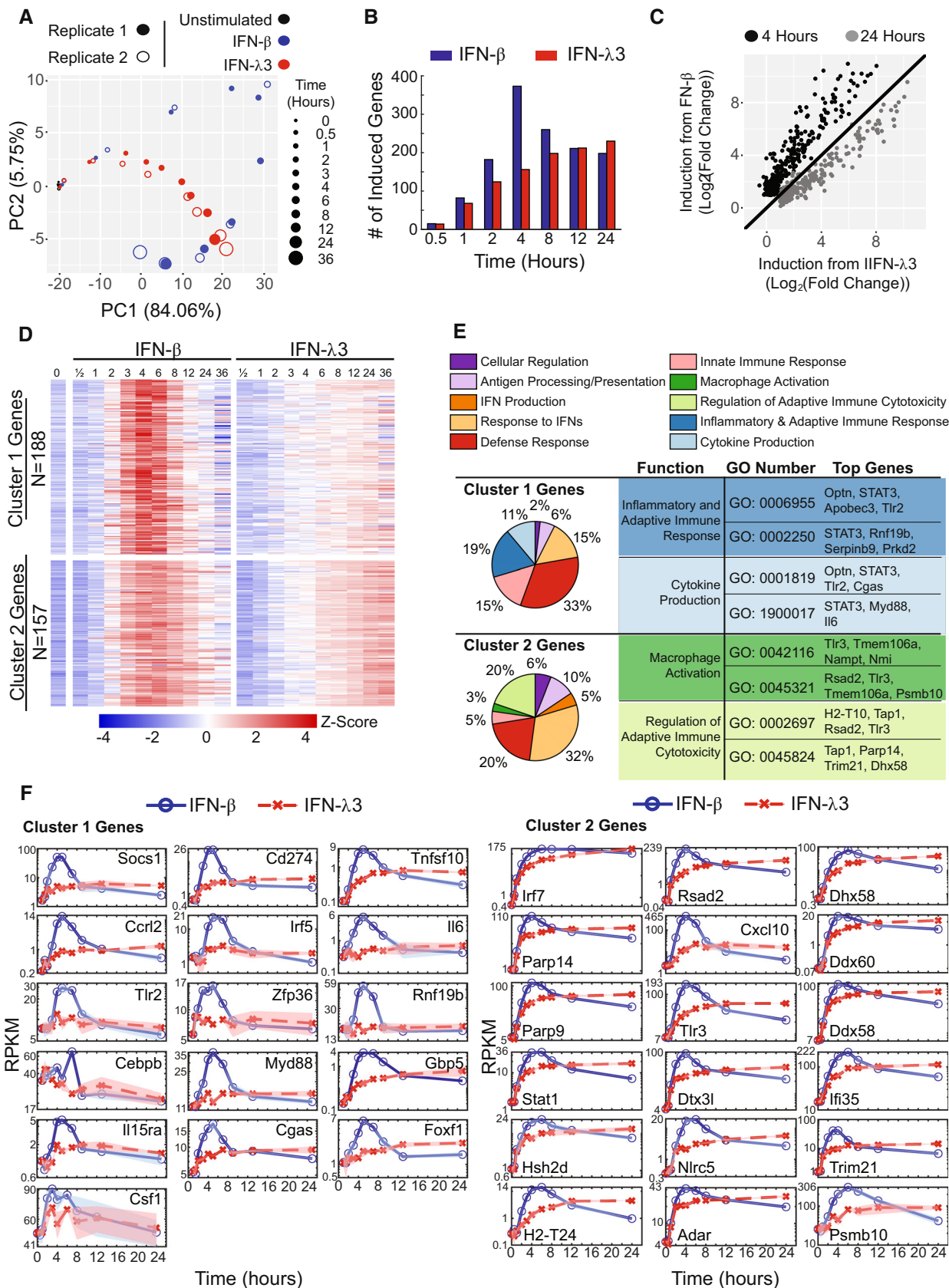
**Figure 1.**

**Figure 1.   IFN-β, but not IFN-λ3, induces an inflammatory gene expression program.**

A   Principal component analysis (PCA) of interferon-response transcriptomes in MLE-12 cells. Replicate datasets (open and closed circles) for IFN-β (10 U/ml, blue) and IFN-λ3 (100 ng/ml, red) describe distinct trajectories over the two-dimensional map of PC1 and PC2, at the indicated times of the time course (increasing circle size). Data are from two independent experiments.

B   Bar graphs of the number of genes induced (log$_2$(FC) ≥ 1, FDR-corrected $P$-value ≤ 0.05) by IFN-β (blue) or IFN-λ3 (red) at each indicated time point.

C   Scatter plot of fold induction in gene expression in response to IFN-λ3 versus IFN-β at an early time point (4 h, black) and a late time point (24 h, gray).

D   Heatmap depicting the scaled mRNA expression time course of individual genes. The gene expression was averaged from two replicates and scaled (Z-score) for each gene in response to IFN-β and IFN-λ3 over time. Mean expression is depicted as white and values above or below the mean depicted as red or blue, respectively. Genes were clustered based on differential gene expression analysis. Genes in cluster 1 are differentially induced during at least one time point by IFN-β (FDR-corrected $P$-value ≤ 0.05), but not IFN-λ3. Cluster 2 contains other genes that are induced by both IFN-β and IFN-λ3 during at least one time point compared with unstimulated.

E   Pie charts of the biological functions of cluster 1 and 2 genes, as determined by Gene Ontology (GO) analysis. Biological programs are depicted in the indicated color code. Example biological functions that are specific to cluster 1 or 2 genes are listed with example GO ID numbers and top, over-represented genes from either cluster that mapped to the indicated GO ID.

F   Line graphs depicting the mRNA expression time course (averaged from two replicates) induced by IFN-β (blue) or IFN-λ3 (red) of indicated genes from cluster 1 and 2. Genes contributing the highest variance to PC1 or PC2 (i.e., upper quartile) from the PCA analysis and that have important biological functions specific to cluster 1 or 2 from the GO analysis are shown plotted with connecting lines.

Source data are available online for this figure.

with gene expression peaking at later time points (12, 24, and 36 h). Gene Ontology (GO) analysis identified potential cluster-specific biological functions such as "inflammatory and adaptive immune response" as well as "cytokine production" for cluster 1 genes and "regulation of adaptive immune cytotoxicity" as well as "macrophage activation" for cluster 2 genes (Fig 1E).

To inspect the expression time course of specific genes with important cluster-specific biological functions in more detail, we selected genes based on top quartile loadings of principal component 2 (Fig 1A; Dataset EV1), presence in cluster 1 (Fig 1D) and association with cluster 1-specific GO functions (i.e., inflammatory and adaptive immune response and cytokine production). Line graphs of these cluster 1 genes confirmed the IFN-β-specific induction around the 4-h time point (Fig 1F). A similar analysis was conducted for the top quartile genes contributing to variance in PC1 that are also found in cluster 2 and contribute to cluster 2-specific biological functions (i.e., regulation of adaptive immune cytotoxicity and macrophage activation). While many of these genes showed higher expression levels with IFN-β at 4 h, with IFN-λ3 they reached almost equivalent expression levels at late time points. Many of these genes (e.g., IRF7, RSAD2, TLR3, DDX58, and IFI35) have been classified as "robust" IFN response genes (Levin et al, 2014).

## Differential ISGF3 temporal dynamics control gene expression programs

Since the temporal expression trajectories of cluster 2 genes were distinct when stimulated with either IFN-β or IFN-λ3, we hypothesized that IFN-specific temporal dynamics of the transcription factor ISGF3 were responsible. To examine this question, we measured ISGF3 activity in a time course of MLE-12 lung epithelial cells incubated with 10 U/ml IFN-β or 100 ng/ml IFN-λ3 using an electrophoretic mobility shift assay (EMSA) with an ISRE oligo probe using constitutive transcription factor NFY as control (Fig 2A). We found three phases of ISGF3 activity during the IFN-β stimulation: an activation phase (0 to 60 min), a potentiated phase (80 min to 4 h), and an inactivation phase (6 to 12 h). IFN-λ3-stimulated ISGF3 shared the activation phase, but lacked the potentiated phase, instead showing a trough (40 min to 2 h), and reactivation phase (4 to 12 h). The IFN-β-specific potentiated phase is characterized by a more than a twofold increase in activity that peaks at 4 h of stimulation.

A simple model, composed of an ordinary differential equation (ODE), was used to determine whether the temporal dynamics of ISGF3 activity might account for the measured cluster-specific expression dynamics in response to each stimulus. The ODE model simulates the change in mRNA abundance as a function of mRNA synthesis activated by the ISGF3 transcription factor with an activation constant ($K_A$), Hill coefficient ($n$), and an mRNA degradation rate constant ($k_{deg}$). The only time-dependent model variable is the ISGF3 activity, quantified from the EMSA (Fig 2A), which was used as an input. The model simulations were fit to the median mRNA abundances for genes in each cluster at each time point for both stimuli (Fig 2B; Dataset EV1) using a simplex search parameter optimization with 50 random initializations. To ensure robustness, the optimization workflow was conducted five times and the mean and associated standard error of the top 10 parameter sets from the five independent runs is reported. As expected, we were able to identify a parameter set that produced good fits for cluster 2 for both stimuli (RMSD = 0.119 ± 0.0001; Fig 2C). Then, using the time course data of cluster 1, we identified a different parameter set that produced model simulations with a good fit (RMSD = 0.152 ± 0.0002). This suggests that the IFN-specific temporal dynamics of ISGF3 activity may be sufficient to mediate not only IFN-specific temporal control of ISG expression (cluster 2) but also activation of an IFN-β-specific gene expression program (cluster 1), without the need to invoke other pathways or transcription factors.

The parameter sets for the models for cluster 1 and 2 differed by 1.2× in the activation constant, by 1.5× in the degradation rate constant, and by 2× in the Hill coefficient. Using a sensitivity analysis where one parameter was changed by a multiplier, we found that for the cluster 1 model a fourfold increase or decrease in the activation constant, $K_A$, diminished the performance of the model only minimally (RMSD = 0.160 and 0.153, respectively; Fig 2D). In contrast, a much smaller range (≥ 0.7× and ≤ 1.4×) for the values of the fitted Hill coefficient, $n$, was found to be necessary in both parameter sets. The cost function more than doubled (RMSD = 0.342) when decreasing the Hill coefficient in the cluster 1 model to 1.0, and more than tripled (RMSD = 0.380) when increasing it to 2.0 in the cluster 2 model. The mRNA degradation constant showed an intermediate sensitivity: a 0.7- and 1.4-fold change for models 1 and 2, respectively, resulting in a slightly increased RMSD (0.173 and 0.153,

**A**



**B**



**C**



| Parameter | Cluster 1 | Cluster 2 |
|---|---|---|
| $K_A$ | 0.21 ± 0.02 | 0.17 ± 0.01 |
| $k_{deg}$ (min$^{-1}$) | 0.0094 ± 0.00012 | 0.0061 ± 0.00001 |
| n | 2.16 ± 0.08 | 1.04 ± 0.00 |
| **Cost function** | | |
| RMSD | 0.152 ± 0.0019 | 0.119 ± 0.00015 |

**D**



**E**



**F**
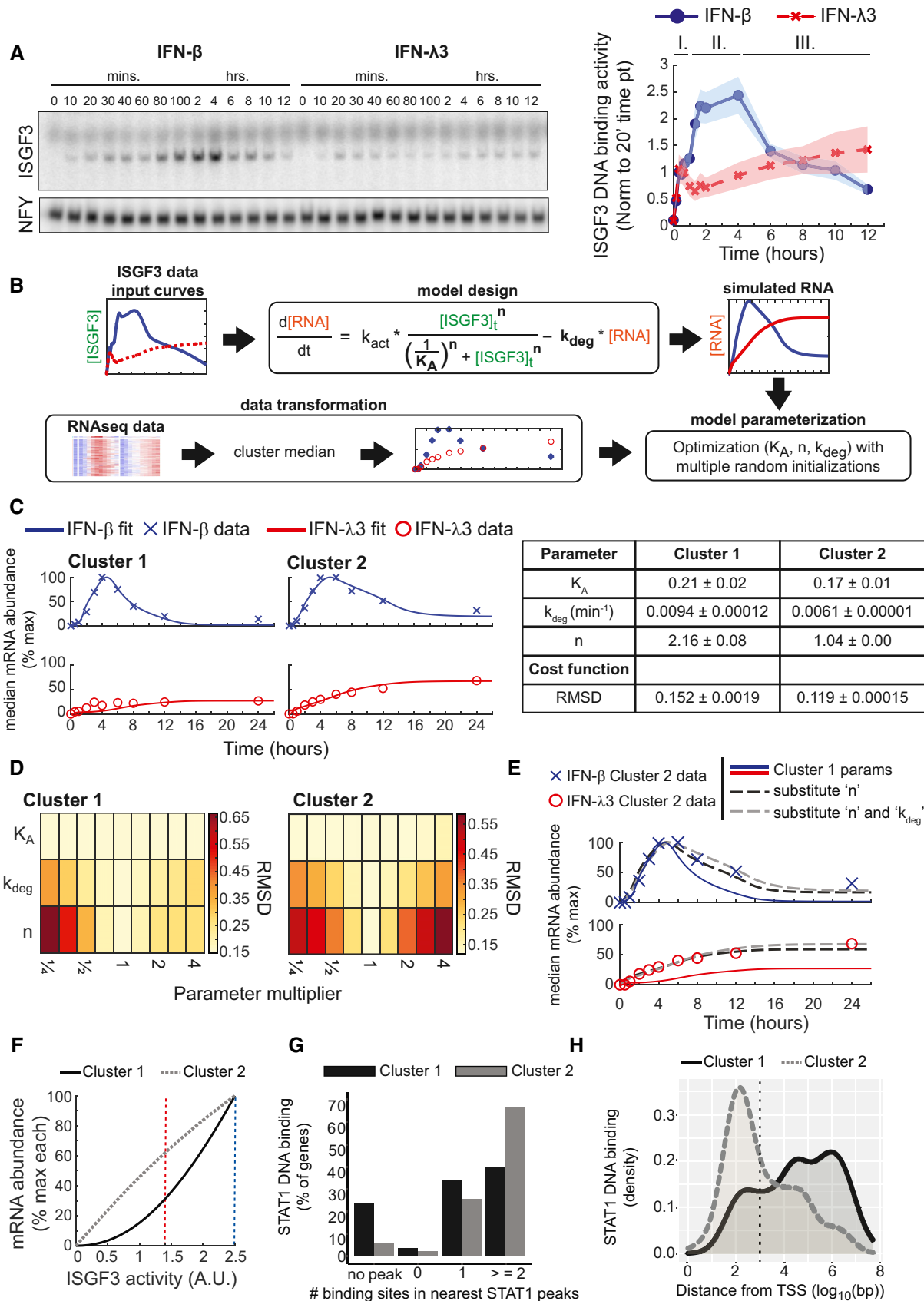


**G**



**H**



**Figure 2.**

**Figure 2. Stimulus-specific temporal dynamics of ISGF3 regulate ISG induction.**

A   ISGF3 activity revealed by an electrophoretic mobility shift assay (EMSA) using nuclear extracts prepared from MLE-12 cells at indicated time points of IFN-β (10 U/ml, blue) and IFN-λ3 (100 ng/ml, red) stimulation. The activity was quantified and normalized to the ISGF3 activity at 20 min of IFN-β stimulation. Line graphs were plotted using connecting lines. Shaded areas on the line graphs depict the standard error of the mean (SEM) from at least five independent experiments. The three phases of ISGF3 activity are indicated above the graphs.

B   Schematic of the ordinary differential equation (ODE) model and optimization pipeline. Quantified ISGF3 curves were used as input data (green text in equation) for an ODE-based model of mRNA expression with a Hill-based production term and degradation term. The model was parameterized by fitting the $K_A$, $k_{deg}$, and $n$ parameters (bold text in equation) to the median mRNA expression levels of cluster 1 and 2 time courses.

C   Line graphs depicting the simulated best-fit model (solid line) for genes in both clusters and the experimental median IFN-β (cross) and IFN-λ3 (open circle) induced gene expression levels at each time point. Simulated and experimental data were normalized to the percentage of the maximum response of both stimuli. The optimized parameter sets and associated standard error of the mean of five optimization runs each represented by the best 10 of 50 resulting from random initializations for cluster 1 and cluster 2 are listed in the table.

D   Heatmap of the root mean square deviation (RMSD) of simulated and experimental mRNA levels when changing parameters ($K_A$, $k_{deg}$, and $n$) by the indicated value with the best-fit models for cluster 1 and cluster 2. Good fits with lower RMSD values are depicted as a pale yellow while larger values indicating poor fits are dark red.

E   Line graphs depicting the simulated best-fit model for cluster 1 (solid line) and the cluster 2 experimental median IFN-β- (cross) and IFN-λ3- (open circle) induced mRNA abundances at each time point. Simulations of the cluster 1 model after substituting the values of the Hill coefficient (black dotted line) or both Hill coefficient and the degradation rate constant (gray dotted line) with the value from the cluster 2 model.

F   Line graphs of an ISGF3 dose–response curve for the cluster 1 and cluster 2 models. The mRNA level for different amounts of ISGF3 activity is plotted for the cluster 1 model (solid black line) and cluster 2 model (dotted gray line). The maximum amount of ISGF3 activity induced by either IFN-β (vertical dashed blue line) or IFN-λ3 (vertical dashed red line) is indicated in the graph.

G   Bar graphs of the number of STAT1 binding motifs for genes in cluster 1 and 2. ChIP-seq analysis of STAT1 binding motifs was identified under STAT1 peaks. Cluster 1 and cluster 2 genes were mapped to the nearest STAT1 binding sites, and the number of motifs under the nearest peak was counted and plotted.

H   Density plots depicting the distance of genes in cluster 1 and 2 to the nearest STAT1 binding site. ChIP-seq analysis of the proportion of STAT1 peaks plotted based on their distance from the nearest gene. STAT1 binding less than or greater than 1,000 base pairs (vertical dotted black line) were classified as either proximal promoter or distal enhancer binding.

Source data are available online for this figure.

respectively). Taken together, this suggests the decoding of ISGF3 temporal dynamics relies on specific values of the Hill coefficient and, to a smaller extent, the mRNA degradation constant.

Given that the cluster 2 model fit poorly to cluster 1 data (RMSD = 0.432), we asked which parameter difference was critically important to distinguish cluster 1 from cluster 2 (Fig 2E). We found that substituting the Hill coefficient alone was sufficient to improve the model performance to more closely simulate the cluster 1 data (RMSD = 0.183). Substituting both the Hill coefficient and degradation rate further improved the fit (RMSD = 0.152). The dose–response relationship of mRNA abundance against ISGF3 activity for the cluster 2 model is close to linear for the experimentally determined range of ISGF3 activity (Fig 2F). For the experimentally measured maximum ISGF3 activity induced by IFN-λ3 (1.4 A.U., red dotted vertical line), the mRNA abundance is 62% compared with the maximum mRNA abundance seen with the measured IFN-β-induced activity (2.5 A.U., blue dotted vertical line). This is in contrast to the cluster 1 model whose nonlinear dose–response results in only 31% mRNA abundance for 1.4 A.U. ISGF3 activity.

The modeling suggested an ultrasensitive dose–response curve for cluster 1 genes versus a linear dose–response curve for cluster 2 genes. Such nonlinear dose–responses may arise from multiple transcription factors binding and synergizing in the activation of the promoter (Johnson *et al*, 1979; Carey *et al*, 1990), or from chromatin looping to connect distal enhancers with promoters (Kuhlman *et al*, 2007; Earnest *et al*, 2013; Hou *et al*, 2018). We investigated each possibility by examining STAT1 ChIP-seq data and identified STAT1 binding motifs within the measured STAT1 peaks. This analysis did not reveal an overrepresentation of multiple motifs in STAT1 peaks associated with cluster 1 genes (Fig 2G). However, many more cluster 1 genes showed larger distances between STAT1 peaks and transcription start sites (TSSs), while for cluster 2 genes

STAT1 peaks tended to be promoter-proximal (Fig 2H). This analysis suggests the possibility that the ultrasensitive dose–response behavior that is driving the type I-specific expression of cluster 1 genes may be mediated by the need to engage in chromatin looping events that connect distal ISGF3 binding to the TSSs of target genes.

## A model of the IFN-ISGF3 signaling network guides experimental studies

Since the IFN-type-specific temporal dynamics of ISGF3 appear to control IFN-specific gene expression levels, we examined the mechanisms for regulating ISGF3 dynamics. We leveraged an ODE model of the JAK–STAT signaling pathway that recapitulates IFN-α-induced signaling in hepatocytes (Kok *et al*, 2020), which contains 41 molecular species connecting ligand-receptor interactions with nuclear ISGF3 activity (Table EV1). To adapt the model to IFN-β-induced ISGF3 signaling in epithelial cells, we produced experimental data from time course measurements of the pathway regulators STAT1, STAT2, IRF9, SOCS1, SOCS3, and USP18 during IFN-β stimulation using immunoblot, EMSA, and qPCR assays (Fig 3A). We sought to make the least number of parameter changes and thus implemented an iterative algorithm starting with only three systematically selected parameters to produce an optimal fit (Fig 3B; Table EV2). However, key features were not captured, such as the potentiated phase of some of the nuclear active species (ISGF3 and pSTAT1), the late phases of the nuclear total species (STAT1, STAT2, IRF9), as well as the dynamics of most of the mRNA species (total RMSE = 73.26; Fig 3C). To improve the model fits, three additional parameters were systematically selected for optimization. We found that allowing 12 parameters to be estimated was sufficient to capture the potentiated phase of the nuclear active species and the late phase of the nuclear inactive species (total RMSE = 43.72), but
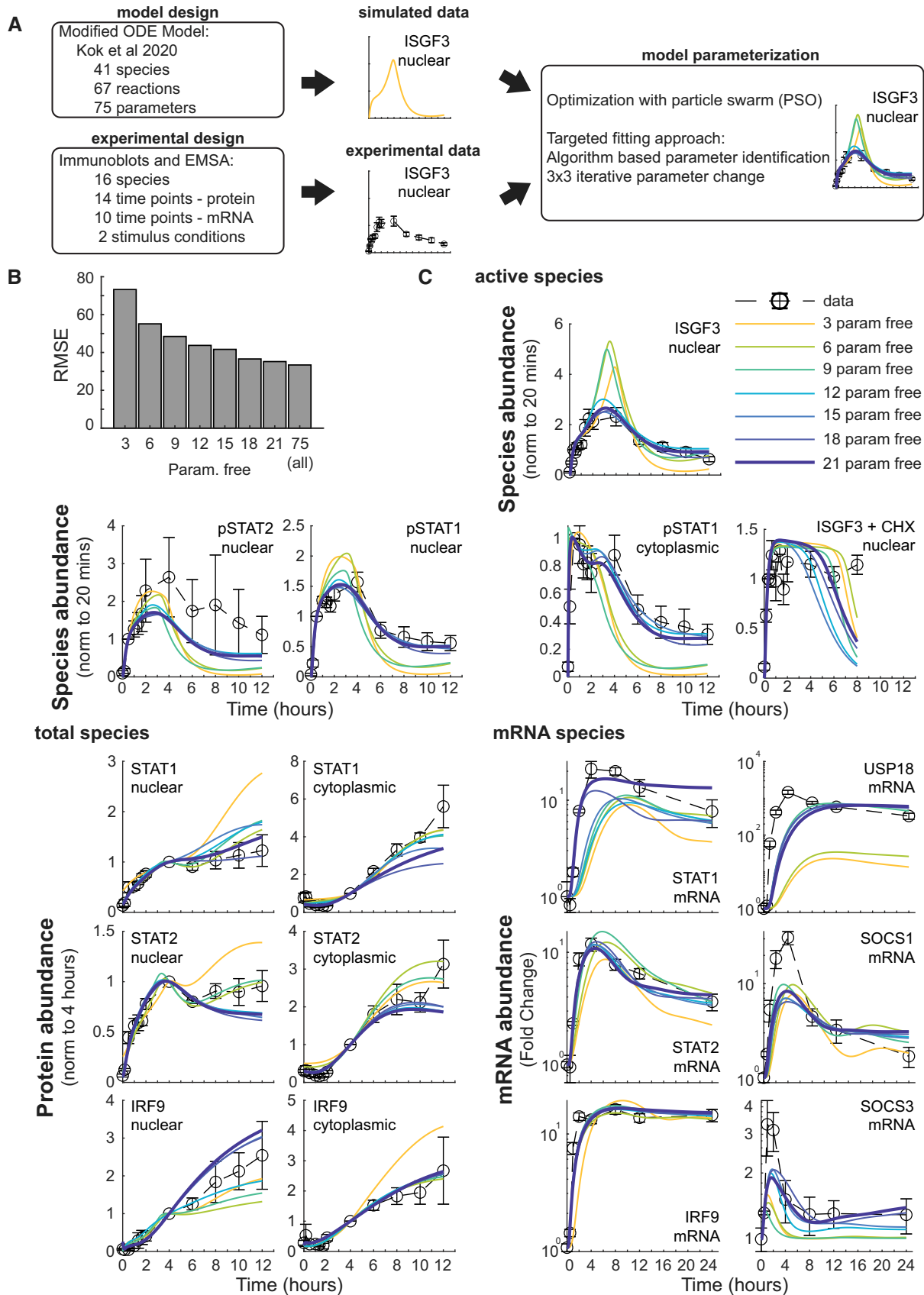
**Figure 3.**

Figure 3.  Applying a dynamical network model to IFN-β-induced lung epithelial cell signaling.

A    IFN signaling network model design and parameterization. A previously published IFN-α signaling model was modified and parameterized using a particle swarm optimization (PSO) to fit simulations to time course data of model species. To minimize alterations to the original model, an iterative approach based on a 3-by-3 parameter identification and fitting was implemented.
B    Bar graph of the root mean square error (RMSE) of optimally fit models compared with experimental data. Models, in which 21 of the 75 parameters are fit, provide an optimal fit.
C    Comparisons of model simulations to time course datasets. Using quantified immunoblot and EMSA time course data (open circles with dotted black line) of nuclear and cytoplasmic active species (ISGF3, phosphorylated STAT1 (pSTAT1), phosphorylated STAT2 (pSTAT2)), total species (STAT1, STAT2, and IRF9), and mRNA species (STAT1, STAT2, IRF9, USP18, SOCS1, and SOCS3) during 10 U/ml IFN-β stimulation, the best-fit model (bold dark blue line) was determined. Visual inspection confirms that 18 or 21 parameter fitting results in satisfactory fits to the experimental data. The SEM of the datasets is depicted from at least three independent experiments.

Source data are available online for this figure.

the 21-parameter estimation further improved the overall fit, particularly the STAT1 mRNA data (total RMSE = 35.18). To avoid overfitting, no larger sets of parameters were tested since the error had reached a plateau, showing a similar error when fitting all the parameters concurrently (total RMSE = 33.38; Fig 3B). The parameter changes (Table EV2) suggest that MLE-12 lung epithelial cells have altered nucleo-cytoplasmic transport to increase the nuclear residence time of ISGF3 and lower STAT1 and 2 expression levels than in the original model that was parameterized to hepatocytes. With the new MLE-12 adapted model (i.e., 21-free-param model), we could now explore the circuit mechanisms that are key to IFN-β-specific ISGF3 dynamics.

Using the signaling model adapted to IFN-β-responding MLE-12 lung epithelial cells, we explored how varying the dose of IFN-β stimulation would affect the temporal dynamics, and specifically, the potentiated phase of ISGF3 activity. First, we decreased the dose of IFN-β by two-, four-, ten-, or twenty-fold (Fig 4A). While 1× IFN-β (50,000 molecules/cell) induced an initial activation phase up to 1 h followed by a potentiated phase up to 4 h, our simulations predicted a dose-dependency in the magnitude of the ISGF3 response. We plotted the ISGF3 activity during the initial activation phase at 1 h and during the potentiated phase at 4 h and found that the potentiated phase is reduced more drastically than the initial activation phase (Fig 4B). For example, the model predicted that a

10-fold lower IFN-β dose would reduce the 4-h activity by about 2.3×, whereas the 1-h activity remained within 1.2× of the original, resulting in close to equal magnitudes at both time points. Experimentally, we tested three doses (10, 1, and 0.1 U/ml) in an ISGF3 time course experiment (Fig 4C). Similar to the model predictions, ISGF3 activity trajectories were diminished at lower doses. The quantified experimental data showed a much more severe reduction in the 4-h potentiated phase than the 1-h activation phase such that both time points had close to equal ISGF3 activity at lower doses (Fig 4D). This suggests that the IFN-β-specific potentiated phase of ISGF3 is dose-dependent and requires a higher dose-range than the initial activation phase, which occurs also at lower doses.

To determine whether the ISGF3 potentiated phase is dependent not only on the dose but also the duration of stimulation, we compared model simulations of the sustained 1× IFN-β condition and a pulse stimulation where IFN-β was set to zero after 15 min (Fig 4E). While the activation phase was similar in both conditions, the potentiated phase did not occur with the shorter stimulation time. Instead, ISGF3 activity rapidly decreased to baseline within 6 h. We tested this prediction experimentally in MLE-12 lung epithelial cells stimulated with 10 U/ml IFN-β for 15 min (Fig 4F). Similar to the model predictions, the experimental ISGF3 activity did not increase after the activation phase but diminished to basal activity by 6 h. Together, the modeling and experimental results suggest that the

Figure 4.  ISGF3 dynamics, which depend on the dose and duration of IFN-β stimulation, control expression of inflammation genes.

A    Line graphs of model simulations of dose-dependent ISGF3 temporal dynamics. Using the adapted IFN signaling model (i.e., the 21-free-param model), simulations predict ISGF3 DNA binding activity at various IFN-β doses (thin solid lines) that are lower than the simulation that was fit to experimental data (thick blue line).
B    Bar graphs of ISGF3 activity during the primary activation (1 h) and secondary potentiated (4 h) phases, as simulated by the model with indicated doses of IFN-β (panel A).
C    Line graphs of experimental dose-dependent ISGF3 temporal dynamics. ISGF3 activity during 10 U/ml, 1 U/ml, and 0.1 U/ml IFN-β stimulation was revealed by an EMSA and quantified. The SEM is depicted from at least two independent experiments.
D    Bar graphs of ISGF3 activity during the primary activation (1 h) and secondary potentiated (4 h) phases, as experimentally determined for indicated doses of IFN-β (panel C). The SEM is depicted from at least two independent experiments.
E    Line graphs of simulated ISGF3 activity during sustained (blue line) and a 15-min pulse (purple line) of IFN-β.
F    Line graphs of experimental ISGF3 activity during sustained (blue line) compared with a 15-min pulse (dashed purple line) of 10 U/ml IFN-β. Data are from at least three independent experiments.
G    PCA of IFN-induced transcriptomes with sustained high (10 U/ml, blue), low (1 U/ml, light blue), or pulse (15 min of 10 U/ml, purple) IFN-β and IFN-λ3 (100 ng/ml, red) stimulus conditions. Trajectories of gene expression levels over time (increasing circle size) are depicted for two independent experiments (open and closed circles). The 4-h time point for each condition is indicated by dashed circles.
H    Heatmap depicting the time course of scaled mRNA abundances of individual genes during IFN stimulus conditions eliciting stimulus-specific ISGF3 temporal dynamics. Mean expression levels for each gene in cluster 1 during IFN-β (10 U/ml), IFN-λ3 (100 ng/ml), low IFN-β (1 U/ml), or pulse IFN-β (15 min of 10 U/ml) are depicted in white, while values above or below the mean are depicted in shades of red or blue, respectively.
I    Line graphs of mRNA abundance time course induced by IFN-β, IFN-λ3, low IFN-β, or pulse IFN-β. Genes selected based on analysis of gene cluster specificity and biological importance from Fig 1F are depicted here with connecting lines.
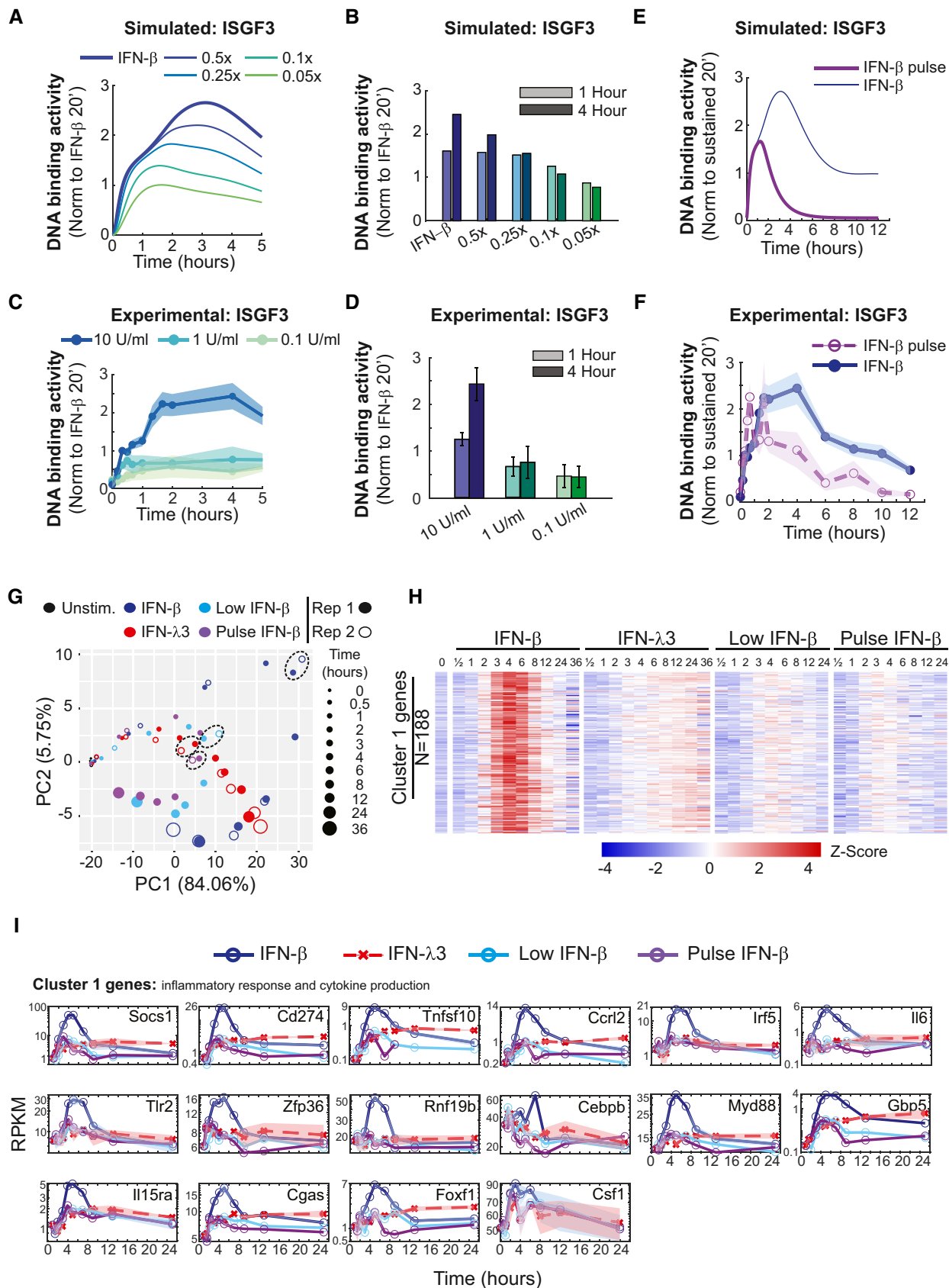
Source data are available online for this figure.

**Figure 4.**

IFN-β-specific potentiated phase of ISGF3 requires higher doses and longer durations of ligand exposure.

The above-described stimulation conditions allowed us to assess the functional consequence of the ISGF3 potentiated phase for gene expression. We isolated RNA from MLE-12 lung epithelial cells incubated with either low IFN-β (1 U/ml) or pulse IFN-β (15 min of 10 U/ml) for various durations and assessed the expression of the previously identified 345 IFN-β inducible genes by RNA-seq. Principal component analysis revealed that the response profile for neither condition converged with the response profile for sustained IFN-β after 1 h, but clustered near the IFN-λ3-induced profile until 4 h (Fig 4G, dashed circles). After 4 h, the pulse and low IFN-β-induced transcriptomes converge toward the unstimulated condition. When examining the previously identified IFN-β-specific gene expression program in cluster 1, the lower dose and shorter duration of IFN-β was not sufficient to induce these genes (Fig 4H). Line graphs of cluster 1-specific inflammatory & adaptive immune response and cytokine production genes (e.g., Cd274, Il6, TNFSF10, CCRL2, Tlr2, Myd88, and IRF5) confirmed that only the sustained and high dose of IFN-β was able to induce them (Fig 4I). This demonstrates that the ISGF3 potentiated phase induced with high and sustained IFN-β stimulation is needed to activate expression of specific genes involved in the regulation of inflammatory and adaptive immune responses, and cytokine production.

### A stimulus-contingent positive feedback loop interprets stimulus dose and duration

Since the ISGF3 potentiated phase has biological importance in regulating a subset of inflammatory genes, we investigated the mechanisms controlling this phase of the ISGF3 response. Given the timing of the response and the dependency on dose and duration, we hypothesized that a stimulus-contingent positive feedback loop was regulating the ISGF3-potentiated phase. To test this, the protein synthesis inhibitor cycloheximide (CHX) was incubated with MLE-12 lung epithelial cells stimulated with IFN-β to block induced feedback loops (Fig 5A). Time course measurements of ISGF3 activity revealed that while the initial phase of ISGF3 activity was not affected by the CHX treatment, the potentiated phase, which starts after the first hour, was blocked. The level of ISGF3 activity induced during the activation phase was sustained throughout the remainder of the time course, suggesting that a positive feedback loop is required to amplify the ISGF3 response. To identify potential gene candidates for the positive feedback amplifier, we measured STAT1, STAT2, and IRF9 mRNA abundances, known positive regulators of IFN signaling, during an IFN-β stimulated time course using RT–qPCR (Fig 5B). By 60 min, IRF9 mRNA had already increased about eightfold, while STAT1 and STAT2 mRNA had doubled at that time. Measuring the nuclear STAT1, STAT2, and IRF9 protein, we also observed that IRF9 had the largest increase (sevenfold) during the potentiated phase (100 min) with respect to the activation phase (30 min) compared with STAT1 (40% increase) and STAT2 (30% increase; Fig 5C). This suggests that IRF9 induction, and to a lesser extent STAT1 and STAT2 induction, acts as a critical positive autoregulation circuit for ISGF3 and is needed for the stimulus-contingent positive feedback loop.

Using the MLE-12 IFN signaling model, we tested how IRF9 as well as STAT2 positive autoregulation during IFN-β stimulation affects ISGF3 activity (Fig 5D). Model simulations predicted that when IRF9 induction is blocked the potentiated phase of the ISGF3 response is reduced, while the activation and late phase are similar to the control. Blocking the STAT2 positive autoregulation reduced the potentiated phase but also the late phase. Eliminating STAT1 autoregulation in the model simulation also eliminated the potentiated and late phases (Fig EV2) but this was not further explored experimentally as STAT1 also participates in other complexes (e.g., GAF) making downstream gene expression effects difficult to interpret. In order to test the model predictions, the ISGF3 binding site

---

**Figure 5. Stimulus-contingent positive feedback loop regulates the ISGF3 potentiated phase and is needed for ISGF3 potentiated-dependent gene induction.**

A   Line graphs of ISGF3 temporal dynamics during inhibition of protein synthesis. The temporal dynamics of ISGF3 activity when stimulated with 10 U/ml IFN-β with (blue line) or without (green dotted line) 10 μg/ml cycloheximide (CHX) was measured by EMSA. The SEM is depicted from at least three independent experiments.

B   Line graphs of mRNA expression levels of positive regulators of IFN signaling. The temporal dynamics of STAT1 (black line), STAT2 (orange line), and IRF9 (purple line) mRNA induction during IFN-β stimulation (10 U/ml) were determined with a time course of gene expression levels measured using qRT–PCR. The SEM is depicted from at least four independent experiments.

C   Bar graphs of nuclear STAT1, STAT2, and IRF9 protein levels during the primary activation phase (30 min) and start of the secondary potentiated (100 min) phase. Nuclear STAT1 (black bars), STAT2 (orange bars), and IRF9 (purple bars) protein abundances were measured using quantified immunoblots of MLE-12 lung epithelial cells stimulated with 10 U/ml IFN-β. Data were normalized to 4 h when the protein levels are more abundant. The SEM is depicted from at least four independent experiments.

D   Line graphs of model simulations of STAT2- and IRF9-feedback loop-dependent ISGF3 temporal dynamics. Using the adapted IFN signaling model (Fig 3), simulations predict ISGF3 binding activity when positive feedback loops for STAT2 (yellow line) and IRF9 (purple line) are inhibited compared with the simulation of the WT model (thick blue line).

E   Bar graphs of mRNA gene expression levels of STAT2 and IRF9 in STAT2 and IRF9 promoter mutants. STAT2 and IRF9 mRNA abundances were measured using RT–qPCR of lentiviral control (blue bars), STAT2 promoter mutant (orange bars), or IRF9 promoter mutant (purple bars) MLE-12 lung epithelial cells stimulated with 10 U/ml IFN-β. Data were normalized to the peak expression level at 4 h of the lentiviral control. The SEM is depicted from at least four independent experiments. Statistics were generated using a Student's t-test.

F   Line graphs of experimental STAT2- and IRF9-feedback loop-dependent ISGF3 temporal dynamics. The temporal dynamics of ISGF3 activity in MLE-12 lung epithelial cells with mutations in the STAT2 promoter (orange dashed line), IRF9 promoter (purple dashed line), or a lentiviral control (black line) when stimulated with 2.77 U/ml IFN-β was measured with an EMSA. The SEM is depicted from at least two independent experiments.

G   Line graphs of mRNA gene expression levels of important inflammatory genes in STAT2 and IRF9 promoter mutants. mRNA abundances of genes selected based on biological importance from Fig 1F are depicted from lentiviral control (blue bars), STAT2 promoter mutant (orange bars), or IRF9 promoter mutant (purple bars) MLE-12 cells stimulated with 10 U/ml IFN-β. Data were normalized to the peak expression level of the lentiviral control. The SEM is depicted from at least three independent experiments.

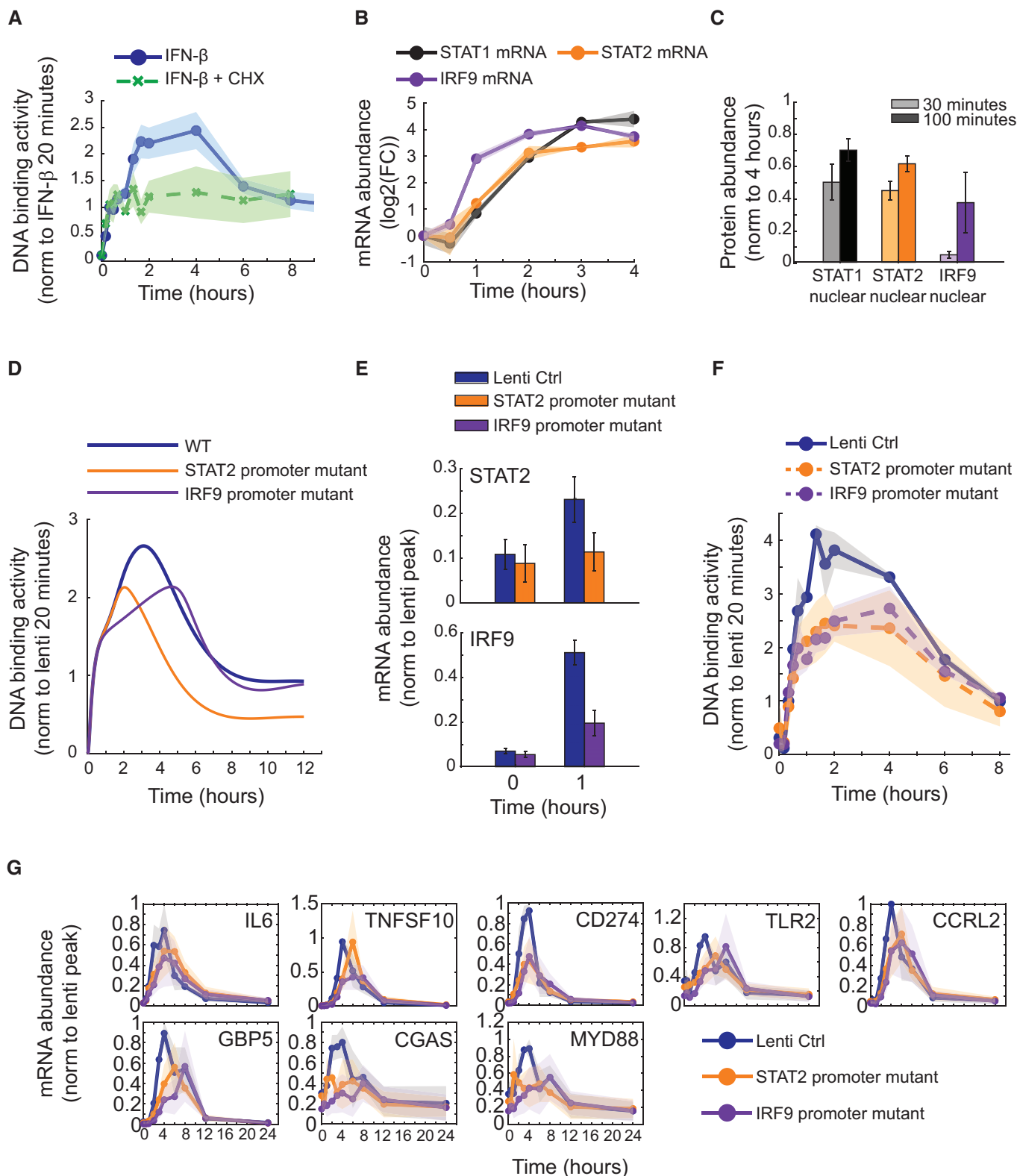Source data are available online for this figure.

**Figure 5.**

within the IRF9 and STAT2 promoters in the MLE-12 lung epithelial cells was mutated using CRISPR-Cas9 gene editing (Fig EV3A). This resulted in mutant variants in 79% of the IRF9 promoter region

amplicons and 91% of the STAT2 promoter region amplicons (Fig EV3B). This significantly diminished IRF9 and STAT2 inducibility by IFN-β, as assessed by RT–qPCR (Fig 5E). While the IRF9

promoter mutant and lentiviral control cells had similar basal levels of IRF9, at 1 h of stimulation the abundance of IRF9 was reduced in the mutant cells compared with the control (*P*-value < 0.01). A similar reduction of STAT2 mRNA expression levels was detected in the STAT2 promoter mutant by 1 h of stimulation (*P*-value < 0.05), suggesting diminished induction of the positive autoregulation in the IRF9 and STAT2 promoter mutants.

To examine the functional consequences of diminished autoregulation, the IRF9 and STAT2 promoter mutant cells were stimulated with IFN-β, and ISGF3 activity at various time points measured using EMSA (Fig 5F). Similar to the model simulation, the potentiated phase was found to be diminished in both the IRF9 and STAT2 promoter mutants compared with the lentiviral control cells. To determine gene expression consequences, the mRNA of inflammatory instigator genes (e.g., IL6 and TNFSF10) as well as inflammatory regulator genes (e.g., CD274, TLR2, CCRL2, GBP5, CGAS, and MYD88) from cluster 1 during IFN-β stimulation was measured with a time course using qRT–PCR (Fig 5G). For the IRF9 promoter mutant, the amount of mRNA abundance was decreased in at least one time point for TNFSF10, CD274, CCRL2, GBP5, and CGAS compared with the lentiviral control (*P*-value < 0.05). For many of the genes including TLR2, MYD88, and GBP5, the peak expression level was diminished and delayed to 8 h. The STAT2 promoter mutant also had a reduction in mRNA abundance for CD274, GBP5, and CGAS (*P*-value < 0.05), with shifts in peak expression for many of the genes compared with the lentiviral control. Taken together, this suggests a role for IRF9 and STAT2 positive autoregulatory feedback loops in controlling inflammatory gene expression responses during IFN-β stimulation.

## Discussion

Here, we report that in lung epithelial cells type I IFN-β induces an antiviral gene expression program similar to type III IFN-λ3 and also a gene expression program that includes the prominent inflammatory instigators IL6, TRAIL, and CCRL2. Using experimental and mathematical modeling, we show that the type I IFN-specific gene expression program is regulated by the temporal dynamics of ISGF3. By adapting a mathematical model of the IFN signaling pathway to epithelial cells, we predicted and then experimentally confirmed the dose and duration dependency of the ISGF3 temporal dynamics necessary for the type I IFN-induced inflammatory gene expression program. We also found that the ISGF3-induced expression of its components, STAT2 and IRF9, constitutes positive feedback loops that are important for regulating ISGF3 temporal dynamics and the gene activation of inflammatory instigators.

Our study emphasizes that the IFN gene expression response is not monolithic but depends on the type, dose, and duration of stimulus exposure. Previous studies have alluded to this by observing that type I and III IFN-induced gene expression in hepatocytes shows different kinetics (Bolen *et al*, 2014; Jilg *et al*, 2014). Using IFNAR and IFNλR overexpressing cells, it was found that IFN-type-specific kinetic differences were not due to the IFN dose or receptor abundance (Pervolaraki *et al*, 2018), but the underlying mechanisms remained obscure. Here, we also identified a group of genes (whose biological functions are primarily in cell-intrinsic innate defenses) in epithelial cells that show differential kinetics in response to type I

and III IFNs. And we identified a group of genes (whose biological functions include cell-extrinsic inflammation-induced immune responses) that show substantially different magnitudes such that they may be described as being expressed stimulus-selectively, specific to high-dose IFN-β exposure. We did not find a repressed gene expression program with either IFN stimulus although IFN-repressed genes (IRepG) have been reported in other experimental systems (Trilling *et al*, 2013; Megger *et al*, 2017).

We then addressed the underlying mechanism for type I IFN-specific gene expression. Our results suggest that the stimulus specificity in gene expression responses may be accounted for by stimulus-specific dynamics of the JAK–STAT/IRF signaling network and need not involve additional pathways that were previously implicated, such as MAPK or NFκB (Pfeffer, 2011; Pervolaraki *et al*, 2017; Mitchell *et al*, 2019; Mazewski *et al*, 2020). We provide evidence that type I and III IFN stimulation results in distinct temporal dynamics of ISGF3; while initial activation is similar, only IFN-β-induced ISGF3 shows a potentiated phase. The response selectivity of cell-extrinsic inflammation-induced immune genes due to differences in ISGF3 temporal dynamics could be recapitulated with a mathematical model by postulating a degree of ultra-sensitivity in ISGF3-promoter interactions. The fact that these genes have a larger distance between their transcription start sites and STAT1 binding sites and thus may require DNA looping during the activation process suggests a plausible explanation for ultra-sensitive, nonlinear dose–responses (Kuhlman *et al*, 2007; Earnest *et al*, 2013; Hou *et al*, 2018). Nevertheless, our analysis also revealed substantial heterogeneity within the gene expression response, such that there may be multiple regulatory mechanisms. For example, a coherent feed-forward loop with ISGF3 and ISGF3-induced IRF1 may play a role (Forero *et al*, 2019). Indeed, a finer gene expression analysis and more IFN stimulation conditions will likely identify additional gene expression patterns, as ultimately every immune response gene is probably subject to unique regulatory control mechanisms (Tong *et al*, 2016; Wang *et al*, 2021).

Our study addresses the molecular mechanisms by which IFN-β-induced IGSF3 temporal dynamics are encoded. Prior mechanistic studies of IFN subtype differences have focused on IFN-receptor affinity measurements: IFN-β has high affinity (IFNAR2: 0.2 nM, IFNAR1: 50 nM; Kalie *et al*, 2008; Schreiber & Piehler, 2015), while type III IFN-λ3 binding affinities for its cognate receptors are weaker (IL10Rβ: 850 nM, IFNλR1: 16 μM). This could play a role in the differential cellular responses as engineered interferon variants can have differential innate immune vs inflammatory effects (Mendoza *et al*, 2017; Yen *et al*, 2022). However, kinetic properties of receptor trafficking, receptor turnover and recycling, ligand half-life, and autoregulation mediated by feedback loops may be just as relevant. While not the focus of this work, negative regulators (e.g., SOCS1, SOCS3, and USP18) of the IFN signaling pathway likely impact the inactivation phases of the ISGF3 temporal dynamics (Kubo *et al*, 2003; Malakhova *et al*, 2006; Blumer *et al*, 2017). Additional analyses of the negative regulatory mechanisms may reveal stimulus-specific differences.

Our iterative systems biology analysis using a quantitative dynamical systems model enabled our studies of ISGF3 regulatory mechanisms (Kok *et al*, 2020) and emphasizes the importance of the feedback loops in tailoring the gene expression response to type, dose, and duration of exposure. The critical role of IRF9 in

determining the magnitude of ISGF3 was previously described (Maiwald *et al*, 2010), but here we provide evidence that autoregulation of ISGF3 mediated by IRF9 and STAT2 results in a positive feedback loop that shapes the stimulus-specific dynamics of ISGF3. Positive feedback loops due to positive autoregulation in transcriptional network motifs are known to determine response times, signal sensitivity and amplification, and system bistability (Xiong & Ferrell, 2003; Mitrophanov & Groisman, 2008; Mitrophanov *et al*, 2010). We demonstrate that autoregulation of ISGF3 results in positive feedback loop characteristics but also functions as a filter to distinguish stimulus duration and dose, akin to a coherent feed-forward loop (Alon, 2007). This occurs because active ISGF3 activates the expression of ISGF3 components (inactive ISGF3) that then require continued kinase activity to produce more active ISGF3 to induce the potentiated phase. A stimulus-contingent positive feedback loop governs in principle other immune response transcription factors, such as NFκB, which induces the expression of its components RelA, cRel, and p50, as well as AP1. This induces the expression of its components Fos and Jun. Our study here may prompt an examination of their dynamical properties to determine whether they also function as filters of dose and duration potentially enabling the stimulus-specific activation of target genes. Finally, other feedback loops may also play a role in specifying the dynamic control of ISGF3, particularly at later times beyond the potentiated phase described here.

Our work characterizes a role for type I IFN-β in cell-extrinsic inflammation through induction of inflammatory instigator genes in epithelial cells. We report that the gene expression of inflammatory regulators IL-6, TNFSF10, the gene that encodes for TNF-related apoptosis-inducing ligand (TRAIL), and CCRL2 is tightly controlled and dependent on potentiated activity of ISGF3. Previous reports have described a link between type I IFNs and IL-6 and TNFSF10 in respiratory illnesses (Hadjadj *et al*, 2020; Galani *et al*, 2021), as the latter induces epithelial cell apoptosis (Chaperot *et al*, 2006; Herold *et al*, 2008; Davidson *et al*, 2014). CCRL2 is a nonsignaling transmembrane receptor that presents chemerin, which recruits leukocytes. The detrimental effects of inflammation are prevented in CCRL2-deficient mice (Schioppa *et al*, 2020).

Precise control of IFN responses is critically important, as misregulation of IFNs can result in immunopathogenesis and autoimmunity or exacerbate the pathogenesis of respiratory viral infections (Baechler *et al*, 2003; Banchereau & Pascual, 2006; Blanco-Melo *et al*, 2020; Hadjadj *et al*, 2020; Galani *et al*, 2021). While high IFN-λ1 levels were associated with lower SARS-CoV-2 viral loads and faster clearance in a cohort of COVID-19 patients (Galani *et al*, 2021), a higher IFN-β-to IFN-λ1 ratio was linked to longer hospitalization. Similarly, in a SARS-CoV-1 infection model late activation of type I IFN contributed to lung pathology and morbidity (Channappanavar *et al*, 2016). This highlights the need to further explore type I IFN cell-extrinsic roles during immunopathogenesis.

Misregulation of IFNs and their signaling responses leading to disease has also been linked to genetic variants. Inborn errors of immunity (IEI) have been identified for genetic variants of STAT1 and IRF9 with mutations causing either gain or loss of function (Tangye *et al*, 2020). Other pathway regulators have also been shown to have variants causing IEI such as JAK1, TYK2, IFNAR1, and IFNAR2 (Tangye *et al*, 2020; Zhang *et al*, 2020; Staels *et al*, 2021). While IEI have been thought to be rare, common single-nucleotide polymorphisms (SNPs) have also been found in TYK2 and IFNAR1 and are associated with improved protection from infection as well as increased risk of autoimmunity (Sugrue *et al*, 2021). The prevalence of such SNPs may account for a wide range of IFN pathway responses among individuals (Su *et al*, 2008; Choudhury *et al*, 2014). It will be of interest to delineate how such variants affect the engagement of the described positive feedback loop. Furthermore, the feedback expression of IRF9 and STAT2 may be subject to epigenetic regulation, such that exposure history could modulate pathway regulation and lead to highly individual immune responses. As the inflammatory gene cluster discriminates between modest and high levels of ISGF3, we would expect that there is more variation in the IFN-inflammatory response axis than the antiviral defense functions of IFN.

Our work suggests that ISGF3 dynamic control may be key to understanding the plethora of specific IFN response functions. It suggests strategies to studying these further, leveraging mathematical modeling to develop increasingly reliable simulations that may be a tool for evaluating the potential impact of individual genetic and epigenetic differences for a new generation of precision medicine.

# Materials and Methods

## Cell culture

MLE-12 lung epithelial cells were obtained from ATCC (#CRL-2110) and cultured in DMEM with 4.5 g/l glucose, L-glutamine, and sodium pyruvate (Corning #10-013-CV) supplemented with 10% fetal bovine serum, 100 IU/ml penicillin, 100 μg/ml streptomycin (Corning #30-002-CI), and 2 mM L-glutamine (Corning #25-005-CI) at 37°C at 5% $CO_2$. For stimulations, MLE-12 cells were incubated with 1 U/ml or 10 U/ml recombinant mouse IFN-β (PBL Assay Science #12401-1) and 100 ng/ml recombinant mouse IL-28B/IFN-λ3 (R&D Systems #1789-ML-025/CF). For select experiments, cells were also incubated with 10 μg/ml cycloheximide (Sigma-Aldrich #C7698) or a vehicle (ethanol) control.

## Protein expression analysis by immunoblotting

Protein from extracts was measured (BioRad DC™ Protein Assay Kit II #5000112), and equal amounts of protein were loaded into a 4–15% gradient polyacrylamide gel (BioRad TGX™ Precast Midi Protein Gel #5671085) and proteins separated based on molecular weight using electrophoresis at 110 V. Proteins were transferred onto a PVDF membrane (Fisher Scientific Immobilon®-P IPVH00010) at 100 V for 1 h. The membrane was incubated for 1 h in 5% bovine serum albumin (BSA; Millipore Sigma #A3059) followed by overnight incubation at 4°C in a primary antibody solution. The following antibodies were used in this study: phospho-STAT1 (pY701.4A) mouse monoclonal IgG2aκ targeting to phosphorylated Tyr701 (Santa Cruz Biotechnology #sc-136229), STAT1 p84/p91 (E-23) rabbit polyclonal IgG with epitope matching near the C terminus (Santa Cruz Biotechnology #sc-346), STAT1 p84/p91 rabbit polyclonal IgG antibody (Cell Signaling #9172), phospho-STAT2 (Tyr689) rabbit polyclonal IgG antibody with epitope matching at phosphorylated Tyr689 (EMD Millipore #07–224), STAT2 (D9J7L) rabbit monoclonal

IgG antibody with epitope corresponding near Leu706 (Cell Signaling #72604), IRF9, clone 6F1-H5, mouse monoclonal $IgG_{2a\kappa}$ antibody with epitope matching the N terminus (EMD Millipore #MABS1920), nuclear matrix protein p84 [EPR5662(2)] rabbit monoclonal antibody mapping with aa350-450 (abcam #ab131268), and αTubulin (B-7) mouse monoclonal IgG2aκ antibody raised against epitope with aa149-448 (Santa Cruz Biotechnology #sc-5286). The membrane was washed in TBS-T (0.5% Tween-20) and incubated in a secondary antibody solution for 1 h at room temperature. The following horseradish peroxidase (HRP)-conjugated secondary antibodies were used for this study: mouse anti-rabbit IgG (L27A9) monoclonal antibody (Cell Signaling #5127), goat anti-rabbit IgG polyclonal antibody (Cell Signaling #7074S), horse anti-mouse IgG polyclonal antibody (Cell Signaling #7076), mouse anti-rabbit IgG monoclonal antibody (Santa Cruz Biotechnology #sc2357), and bovine anti-mouse IgG polyclonal antibody (Santa Cruz Biotechnology #sc2380). The protein bands were resolved by chemiluminescence (Thermo Fisher Scientific SuperSignal West Pico and Femto Chemiluminescent Substrate #34080 and 34095).

## Electrophoretic mobility shift assay

The protocol was used as described previously (Hoffmann et al, 2002; Werner et al, 2005). In brief, nuclear fractions were collected by extraction using a Tris (250 mM Tris, 60 mM KCl, 1 mM EDTA) buffer solution. Equal amounts of nuclear protein were incubated for 30 min in a binding buffer (10 mM Tris-Cl, 50 mM NaCl, 10% glycerol, 1% NP-40, 1 mM EDTA, 0.1 mg/ml Poly (deoxyinosinic-deoxycytidylic) acid sodium salt) with 0.01 pmol P-32 radiolabeled oligo containing the ISRE consensus sequence (ISG15 loci; 5′-GATCCTCGGGAAAGGGAAACCTAAACTGAAGCC-3′; 5′-GGCTTCCAGTTTAGGTTTCCCTTTCCCGAGGATC-3′) or a NFY binding sequence (5′-GATTTTTTCCTGATTGGTTAAA-3′; 5′-ACTTTTAACCAATCAGGAAAAA-3′). Samples were loaded onto a 5% polyacrylamide gel (5% glycerol and TGE buffer [24.8 mM Tris base, 190 mM glycine, 1 mM EDTA]). Bands were resolved using electrophoresis at 200 V. Gels were dried and imaged using an Amersham Typhoon 5 laser scanner (GE Healthcare).

## Gene expression analysis by RT–qPCR

RNA was collected from cells lysed in TRIzol Reagent (Fisher Scientific #15–596-018) and isolated using the Direct-zol RNA Extraction Kit (Zymo Research #R2052). Equal amounts of RNA were reverse transcribed into cDNA using the Iscript™ Reverse Transcription Supermix (BioRad #1708841). Equal volumes of diluted (1:8) cDNA were loaded for qPCR analysis along with the SsoAdvanced Universal SYBR Green Supermix (BioRad #1725272) and 0.5 μM forward and reverse primers for target genes (listed below). Amplification curve thresholds were determined and selected for each primer set.

mSTAT1 (5′-GGCCTCTCATTGTCACCGAA-3′; 5′-TGAATGTGAT GGCCCCTTCC-3′);

mSTAT2 (5′-GTAGAAACCCAGCCCTGCAT-3′; 5′-CTTGTTGCCC TTTCCTGCAC-3′);

mIRF9 (5′-TCTTTGTTCAGCGCCTTTGC-3′; 5′-CTGCTCCATCTGC ACTGTGA-3′);

mSOCS1 (5′-CAACGGAACTGCTTCTTCGC-3′; 5′-AGCTCGAAAA GGCAGTCGAA-3′);

mSOCS3 (5′-CTTTTCTTTGCCACCCACGG-3′; 5′-CCGTTGACAGT CTTCCGACA-3′);

mUSP18 (5′-CTCACATGTTTGTTGGGTCACC-3′; 5′-TGAAATG CAGCAGACAAGGG-3′);

mTNFSF10 (5′-GATGAAGCAGCTGCAGGACAAT-3′; 5′-CTGCAA GCAGGGTCTGTTCAAG-3′);

mCD274 (5′-TCGCCTGCAGATAGTTCCCAAA-3′; 5′-GTAAACG CCCGTAGCAAGTGAC-3′);

mCCRL2 (5′-GAGCAAGGACAGCCTCCGAT-3′; 5′-CCACTGTTGT CCAGGTAGTCGT-3′);

mGBP5 (5′-TGCTGACATGAGCTTCTTCCCA-3′; 5′-TCATCGCTA CCTTGCTTCAGCT-3′);

mCGAS (5′-TGGGCACAAAAGTGAGGACCAA-3′; 5′-CGCCAGGT CTCTCCTTGAAAACT-3′);

mMYD88 (5′-TCTCCAGGTGTCCAACAGAAGC-3′; 5′-TGCAAGGG TTGGTATAGTCGCA-3′);

mTLR2 (5′-GGGGCTTCACTTCTCTGCTT-3′; 5′-AGCATCCTCTG AGATTTGACG-3′);

mIL6 (5′-ACCAGAGGAAATTTTCAATAGGC-3′; 5′-TGATGCACTT GCAGAAAACA-3′);

mGAPDH (5′-AGCTTGTCATCAACGGGAAG-3′; 5′-TTTGATGTT AGTGGGGTCTCG-3′).

## RNA sequencing and data analysis

RNA was collected from cells lysed in TRIzol Reagent (Fisher Scientific #15–596-018) and isolated using the Direct-zol RNA Extraction Kit (Zymo Research #R2052). RNA libraries were generated using the KAPA Stranded mRNA-Sequencing Kit with KAPA mRNA Capture Beads (Roche #07962207001). Samples were enriched for poly(A) + mRNA strands using mRNA Capture Beads. The captured mRNA was synthesized into complimentary DNA (cDNA). cDNA libraries were ligated using Illumina TruSeq single index adapters (Roche #KK8700), amplified, and quantified using a Qubit dsDNA Broad Range Assay Kit (Life Technologies #Q32850) and a Qubit 2.0 fluorometer. Sequencing was conducted on an Illumina HiSeq 2500 with single-end 50 bp reads through the UCLA Broad Stem Cell Research Center. Sequencing reads were aligned and mapped onto the mm10 genome. The EdgeR package (Bioconductor 3.7) was used for differential gene expression analysis of raw read counts, which were normalized using trimmed mean of the mean (TMM) and filtered by the number of mapped reads and gene length (RPKM) of greater than 2. Normalized counts were applied to a negative binomial generalized linear model, which was used to calculate biological coefficients of variation. Pairwise dispersions between the normalized counts were calculated using the Cox-Reid Likelihood profile method. The differential expression testing was initiated using the likelihood ratio test (LRT), a form of ANOVA testing. Using the TREAT Method and Benjamini–Hochberg multiple test correction, significantly induced genes were selected based on differences in RPKM values at each time point compared with values in unstimulated conditions using a false discovery rate (FDR) of less than 0.05 based on replicate data and fold change greater than 2. PCA plots were generated using the prcomp function in R and plotted with ggplot2 (Gómez-Rubio, 2017). Correlation plots were plotted using ggplot2. Heatmaps were generated using the pheatmap package.

## ChIP sequencing and data analysis

The protocol was used as described previously (Kishimoto et al, 2021). In brief, cells were fixed with 2 mM disuccinimidyl glutarate for 30 min followed by a 10-min incubation in 1% formaldehyde. Cells are lysed (Buffer 1: 50 mM HEPES-KOH, 140 mM NaCl, 1 mM EDTA, 10% glycerol, 0.5% NP-40, 0.25% Triton X-100, and 1X protease inhibitor cocktail (Thermo Fisher Scientific); Buffer 2: 10 mM Tris–HCl, 200 mM NaCl, 1 mM EDTA, 0.5 mM EGTA, and 1X protease inhibitor cocktail; Buffer 3: 10 mM Tris–HCl, 100 mM NaCl, 1 mM EDTA, 0.5 mM EGTA, 0.1% Na Deoxycholate, 0.5% N-lauroylsarcosine, and 1X protease inhibitor cocktail) and sonicated to shear the chromatin. The DNA-bound complexes were incubated with STAT1 p84/p91 rabbit polyclonal IgG antibody (Cell Signaling #9172) overnight at 4°C. STAT1 was immunoprecipitated by incubating for 5 h at 4°C with Protein-G DynaBeads (Invitrogen #10004D). DNA bound to STAT1 complexes was extracted using 1% SDS and 0.6 mg/ml of Proteinase K (New England Biolabs #P81075) at 60°C overnight, followed by purification with Agencourt AMPure XP solid-phase reversible immobilization (SPRI) beads (Beckman Coulter #A63881). DNA was quantified using a Qubit dsDNA High Sensitivity Assay Kit (Life Technologies #Q32851) and a Qubit 2.0 fluorometer. Libraries were prepared using NEBNext Ultra II DNA Library Prep Kit NEBNext Multiplex Oligos (New England Biolabs) according to the manufacturer instructions and sequenced with a length of 50 bp on an Illumina HiSeq 2500 at the UCLA Broad Stem Cell Research Center. Sequencing data were aligned to mm10 genome as described previously (Kishimoto et al, 2021). MACS2 version 2.1.0 was used to identify peaks for each sample using pooled input samples as control with FDR < 0.01 and extension size of average fragment length (Zhang et al, 2008). STAT1 motifs were identified by searching the HOMER database for position-weighted matrix files of STAT/GAS and ISRE/IRF motifs (Heinz et al, 2010). ISRE/IRF motifs included motifs for T1ISRE, ISRE, IRF2, IRF1, IRF3, and IRF8. STAT/GAS motifs included motifs for STAT1, STAT3 + IL-21, STAT3, STAT4, and STAT5. A variant GAS motif in the promoter of Irf1 (GATTTCCCCGAATG) known to be bound by STAT1 was also included in the search as a GAS motif (Decker et al, 1991). Peak-to-gene distances were calculated with bedtools, using the TSS of the longest isoform (Quinlan & Hall, 2010).

## Gene ontology analysis

The maximum RPKM value and gene names for the selected 188 genes in cluster 1 were analyzed using the Panther Classification System Database DOI: 10.5281/zenodo.4495804 Released 2021-02-01 (Mi et al, 2019). The genes were mapped to the mm10 genome and analyzed using the statistical overrepresentation test, which determines overrepresentation of gene ontology annotations in cluster 1 compared with all expressed genes using the Fisher's exact test and FDR correction. A list of GO biological process terms and IDs as well as associated genes was generated. Each GO term was categorized into 10 groups based on function. To determine whether a function was enriched in a gene cluster the fraction of GO terms for each biological function compared with the total number of terms for the cluster was calculated and plotted as a pie graph. Similar analysis was conducted on the 157 genes in cluster 2.

## Lentiviral cloning, transfection, and infection

The cloning strategy for the lentiCRISPRv2 plasmid was used (Sanjana et al, 2014; Shalem et al, 2014). Briefly, the following oligos were annealed and cloned into a BsmBI (Thermo Fisher Scientific #FD0454)-digested lentiCRISPRv2 vector: STAT2 promoter mutant (5′-CACCGAGGGAAAGGAAACTGAAACC-3′; 5′-AAACGG TTTCAGTTTCCTTTCCCTC-3′); IRF9 promoter mutant (5′-CACCGA CTCAGACCACGTGGTTTCT-3′; 5′-AAACAGAAACCACGTGGTCTGA GTC-3′). Plasmids were transformed into One Shot™ Stbl3™ Chemically Competent bacteria (Thermo Fisher Scientific #C737303). Single colonies were selected and inoculated in LB Broth. Plasmids were isolated from expanded bacterial colonies using the ZymoPURE™ II Plasmid Kit (Zymo Research #D4203). Ten μg of isolated plasmid was transfected into HEK293T cells using Lipofectamine® 2000 Transfection Reagent (Invitrogen #11668–019). Two days following transfection, viral particles were isolated from the HEK293T-conditioned media. MLE-12 lung epithelial cells were infected with the purified viral particles for 24 h, followed by 2 μg/ml puromycin antibiotic selection.

## Sanger and amplicon sequencing

Sequence mutations in the IRF9 and STAT2 promoter mutant cells were confirmed using Sanger sequencing. In brief, 50 ng of genomic DNA (gDNA) was amplified using PCR with 0.5 μM of forward and reverse primers: STAT2 promoter mutant (5′-CCTAT CCTAAGGGACGCAGG-3′; 5′-GCCCAACTAAAGTCTTAGCC-3′); IRF9 promoter mutant (5′-CAAGGTGCTACTGCTGACTG-3′; 5′-TTTCTGAT CTCTCCTCCCC-3′). PCR amplicons were resolved on 2% agarose gels and DNA extracted using the QIAquick Gel Extraction Kit (Qiagen #28706). Ten ng amplicons with 5 μM primers were submitted for sanger sequencing to Laragen, Inc. To quantify the number of sequence variants in the IRF9 and STAT2 promoter mutant cells, PCR amplicons (500 ng) were submitted for Amplicon-EZ sequencing to Genewiz®.

## Mathematical modeling of interferon-induced gene expression

An ordinary differential equation (ODE) mathematical model was built to simulate RNA abundance levels as a function of transcription factor binding and RNA degradation. Briefly, the median RPKM values for all genes within each cluster from the RNA sequencing data were calculated for each time point. The temporal gene expression trajectory of the median values was generated using a modified Akima interpolant fit (MATLAB). The model was composed of four parameters (e.g., $k_{act}$, activation rate; $k_{deg}$, mRNA degradation rate, $K_a$, association constant, and $n$, Hill coefficient). The model was parameterized by model fitting to the gene expression trajectories normalized to max peak. For optimization, the simplex search method (e.g., fminsearch) was implemented using an objective function of the sum of RMSD values calculated at each time point. Fifty multiple random seeds for the initial parameter values were used to optimize over a larger parameter space. The parameter optimization was run 5 times, and the top 10 parameter sets with the lowest RMSD values were averaged and used as the optimized model parameter values. Heatmaps and line graphs were plotted using MATLAB.

### Mathematical modeling of the interferon signaling network

We used the previously published model of interferon signaling (Kok *et al*, 2020), with minor modifications. We replaced the equation for the active receptor complex formation by

$$Bind_{IRF9} \cdot IFN \cdot Rec \cdot \frac{1}{1 + k_{inhBySOCS3} \cdot SOCS3} \cdot \frac{1}{1 + k_{inhBySOCS1} \cdot SOCS1}$$
$$\cdot \frac{1}{1 + k_{inhByUSP18} \cdot USP18}$$

instead of

$$Bind_{IRF9} \cdot IFN \cdot Rec \cdot \frac{1}{SOCS3} \cdot \frac{1}{1 + k_{inhBySOCS} \cdot SOCS1}$$
$$\cdot \frac{1}{1 + k_{inhByUSP18} \cdot USP18}$$

to be able to simulate the model in presence of cycloheximide which blocks protein synthesis, leading to SOCS protein decay, ultimately converging to 0. To better fit our data, we moved the delay term prior to mRNA synthesis instead prior to protein synthesis.

### Parameterization

There are 41 molecular species in the mathematical model (Table EV1). The model parameters (Table EV2) were fit to the data, optimizing parameter value as well as which parameter to change iteratively 3 by 3 in order to adjust the minimal number of parameters allowing for a good fit. Parameters were selected at each iteration by the algorithm based on optimizing the best fit. For comparison, a particle swarm optimization algorithm (740 particles) was used to fit all parameters concurrently.

### Pseudocode

1. Initialize set of indices $I_{-1} = \{\}$
2. For k ranging from 0 to ...

  a. $Cost_k = \infty$
  b. For run ranging from 1 to 20

    i. Optimize the cost function for $\theta = (i_{3k+1}, i_{3k+2}, i_{3k+3}, v_1, \ldots, v_{3k+3})$ using particle swarm optimization with a number of particles equals to $10\times$ the size of $\theta$ ($= 10 \times (3k+6)$).

     • $i_{3k+1}, i_{3k+2}, i_{3k+3}$ correspond to the indices of additional parameters to change,
     • $v_1, \ldots, v_{3k}$ corresponds to the values for previously chosen parameters, that is, with indices from $I_{k-1}$,
     • $v_{3k+1}, v_{3k+2}, v_{3k+3}$ corresponds to the values of parameters $i_{3k+1}, i_{3k+2}, i_{3k+3}$.

    ii. If $cost_{run} < Cost_k$:

     • $I_k = I_{k-1} \cup \{i_{3k+1}, i_{3k+2}, i_{3k+3}\}$
     • $V_k = (v_1, \ldots, v_{3k+3})$
     • $Cost_k = cost_{run}$

  c. If $Cost_k > Cost_{k-1}$

    i. Run step b. with more particles number: $20\times$ size of $\theta$.

3. Return $I_k$ and $V_k$

The cost function was the sum of the mean square error of each individual experiment, as follows:

$$Cost = \sum_{experiments} MSE_{experiment}$$

with

$$MSE_{experiment} = \frac{1}{n_{timepoints}} \sum_{t \in timepoints} \frac{\left(y_{sim}(t) - \overline{y_{obs}(t)}\right)^2}{\sigma^2_{\overline{y_{obs}(t)}}}$$

and with $y_{sim}$ corresponding to simulated outputs for a specific parameter set.

### Implementation

The modeling and parameter optimization were done in MATLAB R2018a using the particleswarm function implemented in MATLAB's optimization toolbox.

## Data availability

Biochemical data from electrophoretic mobility shift assays and immunoblots can be found in the Appendix. The RNAseq datasets and mathematical models presented in this study can be found in online repositories, as follows: GSE219283 (https://www.ncbi.nlm.nih.gov/geo/query/acc.cgi?acc=GSE219283) and GSE161475 (https://www.ncbi.nlm.nih.gov/geo/query/acc.cgi?acc=GSE161475) as well as https://github.com/signalingsystemslab/IFN-GeneRegulation and https://github.com/signalingsystemslab/IFN-signaling.

**Expanded View** for this article is available online.

### Author contributions

**Catera L Wilder:** Conceptualization; formal analysis; investigation; visualization; methodology; writing – original draft; project administration; writing – review and editing. **Diane Lefaudeux:** Formal analysis; methodology; writing – review and editing. **Raisa Mathenge:** Formal analysis. **Kensei Kishimoto:** Formal analysis; investigation; writing – review and editing. **Alma Zuniga Munoz:** Investigation. **Minh A Nguyen:** Formal analysis. **Aaron S Meyer:** Supervision; writing – review and editing. **Quen J Cheng:** Formal analysis; investigation; writing – review and editing. **Alexander Hoffmann:** Conceptualization;

supervision; funding acquisition; writing — original draft; writing — review and editing.

## Disclosure and competing interests statement

The authors declare no conflicts of interest. AH is an EAB member. This has no bearing on the editorial consideration of this article for publication.

# References

(2021) *Coronavirus disease 2019 (COVID-19) treatment guidelines.* Bethesda, MD: National Institutes of Health

Alon U (2007) Network motifs: theory and experimental approaches. *Nat Rev Genet* 8: 450–461

Ank N, West H, Bartholdy C, Eriksson K, Thomsen AR, Paludan SR (2006) Lambda interferon (IFN-lambda), a type III IFN, is induced by viruses and IFNs and displays potent antiviral activity against select virus infections *in vivo. J Virol* 80: 4501–4509

Ank N, Iversen MB, Bartholdy C, Staeheli P, Hartmann R, Jensen UB, Dagnaes-Hansen F, Thomsen AR, Chen Z, Haugen H *et al* (2008) An important role for type III interferon (IFN-lambda/IL-28) in TLR-induced antiviral activity. *J Immunol* 180: 2474–2485

Baechler EC, Batliwalla FM, Karypis G, Gaffney PM, Ortmann WA, Espe KJ, Shark KB, Grande WJ, Hughes KM, Kapur V *et al* (2003) Interferon-inducible gene expression signature in peripheral blood cells of patients with severe lupus. *Proc Natl Acad Sci U S A* 100: 2610–2615

Bancherau J, Pascual V (2006) Type I interferon in systemic lupus erythematosus and other autoimmune diseases. *Immunity* 25: 383–392

Blanco-Melo D, Nilsson-Payant BE, Liu WC, Uhl S, Hoagland D, Møller R, Jordan TX, Oishi K, Panis M, Sachs D *et al* (2020) Imbalanced host response to SARS-CoV-2 drives development of COVID-19. *Cell* 181: 1036–1045.e9

Blumer T, Coto-Llerena M, Duong FHT, Heim MH (2017) SOCS1 is an inducible negative regulator of interferon λ (IFN-λ)-induced gene expression *in vivo. J Biol Chem* 292: 17928–17938

Bolen CR, Ding S, Robek MD, Kleinstein SH (2014) Dynamic expression profiling of type I and type III interferon-stimulated hepatocytes reveals a stable hierarchy of gene expression. *Hepatology* 59: 1262–1272

Carey M, Lin YS, Green MR, Ptashne M (1990) A mechanism for synergistic activation of a mammalian gene by GAL4 derivatives. *Nature* 345: 361–364

Channappanavar R, Fehr AR, Vijay R, Mack M, Zhao J, Meyerholz DK, Perlman S (2016) Dysregulated type I interferon and inflammatory monocyte-macrophage responses cause lethal pneumonia in SARS-CoV-infected mice. *Cell Host Microbe* 19: 181–193

Chaperot L, Blum A, Manches O, Lui G, Angel J, Molens JP, Plumas J (2006) Virus or TLR agonists induce TRAIL-mediated cytotoxic activity of plasmacytoid dendritic cells. *J Immunol* 176: 248–255

Choudhury A, Hazelhurst S, Meintjes A, Achinike-Oduaran O, Aron S, Gamieldien J, Jalali Sefid Dashti M, Mulder N, Tiffin N, Ramsay M (2014) Population-specific common SNPs reflect demographic histories and highlight regions of genomic plasticity with functional relevance. *BMC Genomics* 15: 437

Crotta S, Davidson S, Mahlakoiv T, Desmet CJ, Buckwalter MR, Albert ML, Staeheli P, Wack A (2013) Type I and type III interferons drive redundant amplification loops to induce a transcriptional signature in influenza-infected airway epithelia. *PLoS Pathog* 9: e1003773

Davidson S, Crotta S, McCabe TM, Wack A (2014) Pathogenic potential of interferon αβ in acute influenza infection. *Nat Commun* 5: 3864

Decker T, Lew DJ, Darnell JE Jr (1991) Two distinct alpha-interferon-dependent signal transduction pathways may contribute to activation of transcription of the guanylate-binding protein gene. *Mol Cell Biol* 11: 5147–5153

Dellgren C, Gad HH, Hamming OJ, Melchjorsen J, Hartmann R (2009) Human interferon-lambda3 is a potent member of the type III interferon family. *Genes Immun* 10: 125–131

Earnest TM, Roberts E, Assaf M, Dahmen K, Luthey-Schulten Z (2013) DNA looping increases the range of bistability in a stochastic model of the lac genetic switch. *Phys Biol* 10: 026002

Feld JJ, Kandel C, Biondi MJ, Kozak RA, Zahoor MA, Lemieux C, Borgia SM, Boggild AK, Powis J, McCready J *et al* (2021) Peginterferon lambda for the treatment of outpatients with COVID-19: a phase 2, placebo-controlled randomised trial. *Lancet Respir Med* 9: 498–510

Forero A, Ozarkar S, Li H, Lee CH, Hemann EA, Nadjsombati MS, Hendricks MR, So L, Green R, Roy CN *et al* (2019) Differential activation of the transcription factor IRF1 underlies the distinct immune responses elicited by type I and type III interferons. *Immunity* 51: 451–464.e56

Galani IE, Triantafyllia V, Eleminiadou EE, Koltsida O, Stavropoulos A, Manioudaki M, Thanos D, Doyle SE, Kotenko SV, Thanopoulou K *et al* (2017) Interferon-lambda mediates non-redundant front-line antiviral protection against influenza virus infection without compromising host fitness. *Immunity* 46: 875–890.e76

Galani IE, Rovina N, Lampropoulou V, Triantafyllia V, Manioudaki M, Pavlos E, Koukaki E, Fragkou PC, Panou V, Rapti V *et al* (2021) Untuned antiviral immunity in COVID-19 revealed by temporal type I/III interferon patterns and flu comparison. *Nat Immunol* 22: 32–40

Gómez-Rubio V (2017) ggplot2 - elegant graphics for data analysis (2nd edn). *J Stat Softw* 77: 1–3

Hadjadj J, Yatim N, Barnabei L, Corneau A, Boussier J, Smith N, Péré H, Charbit B, Bondet V, Chenevier-Gobeaux C *et al* (2020) Impaired type I interferon activity and inflammatory responses in severe COVID-19 patients. *Science* 369: 718–724

Heinz S, Benner C, Spann N, Bertolino E, Lin YC, Laslo P, Cheng JX, Murre C, Singh H, Glass CK (2010) Simple combinations of lineage-determining transcription factors prime cis-regulatory elements required for macrophage and B cell identities. *Mol Cell* 38: 576–589

Hemann EA, Green R, Turnbull JB, Langlois RA, Savan R, Gale M Jr (2019) Interferon-λ modulates dendritic cells to facilitate T cell immunity during infection with influenza A virus. *Nat Immunol* 20: 1035–1045

Herold S, Steinmueller M, von Wulffen W, Cakarova L, Pinto R, Pleschka S, Mack M, Kuziel WA, Corazza N, Brunner T *et al* (2008) Lung epithelial apoptosis in influenza virus pneumonia: the role of macrophage-expressed TNF-related apoptosis-inducing ligand. *J Exp Med* 205: 3065–3077

Hoffmann A, Levchenko A, Scott ML, Baltimore D (2002) The IkappaB-NF-kappaB signaling module: temporal control and selective gene activation. *Science* 298: 1241–1245

Hou J, Zeng W, Zong Y, Chen Z, Miao C, Wang B, Lou C (2018) Engineering the ultrasensitive transcription factors by fusing a modular oligomerization domain. *ACS Synth Biol* 7: 1188–1194

Israelow B, Song E, Mao T, Lu P, Meir A, Liu F, Alfajaro MM, Wei J, Dong H, Homer RJ *et al* (2020) Mouse model of SARS-CoV-2 reveals inflammatory role of type I interferon signaling. *J Exp Med* 217: e20201241

Ivashkiv LB (2018) IFNγ: signalling, epigenetics and roles in immunity, metabolism, disease and cancer immunotherapy. *Nat Rev Immunol* 18: 545–558

Ivashkiv LB, Donlin LT (2014) Regulation of type I interferon responses. *Nat Rev Immunol* 14: 36–49

Jagannathan P, Andrews JR, Bonilla H, Hedlin H, Jacobson KB, Balasubramanian V, Purington N, Kamble S, de Vries CR, Quintero O *et al* (2021) Peginterferon lambda-1a for treatment of outpatients with uncomplicated COVID-19: a randomized placebo-controlled trial. *Nat Commun* 12: 1967

Jaks E, Gavutis M, Uzé G, Martal J, Piehler J (2007) Differential receptor subunit affinities of type I interferons govern differential signal activation. *J Mol Biol* 366: 525–539

Jilg N, Lin W, Hong J, Schaefer EA, Wolski D, Meixong J, Goto K, Brisac C, Chusri P, Fusco DN *et al* (2014) Kinetic differences in the induction of interferon stimulated genes by interferon-α and interleukin 28B are altered by infection with hepatitis C virus. *Hepatology* 59: 1250–1261

Johnson AD, Meyer BJ, Ptashne M (1979) Interactions between DNA-bound repressors govern regulation by the lambda phage repressor. *Proc Natl Acad Sci U S A* 76: 5061–5065

Jordan WJ, Eskdale J, Boniotto M, Rodia M, Kellner D, Gallagher G (2007) Modulation of the human cytokine response by interferon lambda-1 (IFN-lambda1/IL-29). *Genes Immun* 8: 13–20

Kalie E, Jaitin DA, Podoplelova Y, Piehler J, Schreiber G (2008) The stability of the ternary interferon-receptor complex rather than the affinity to the individual subunits dictates differential biological activities. *J Biol Chem* 283: 32925–32936

Kishimoto K, Wilder CL, Buchanan J, Nguyen M, Okeke C, Hoffmann A, Cheng QJ (2021) High dose IFN-β activates GAF to enhance expression of ISGF3 target genes in MLE12 epithelial cells. *Front Immunol* 12: 651254

Kok F, Rosenblatt M, Teusel M, Nizharadze T, Gonçalves Magalhães V, Dächert C, Maiwald T, Vlasov A, Wäsch M, Tyufekchieva S *et al* (2020) Disentangling molecular mechanisms regulating sensitization of interferon alpha signal transduction. *Mol Syst Biol* 16: e8955

Kubo M, Hanada T, Yoshimura A (2003) Suppressors of cytokine signaling and immunity. *Nat Immunol* 4: 1169–1176

Kuhlman T, Zhang Z, Saier MH Jr, Hwa T (2007) Combinatorial transcriptional control of the lactose operon of *Escherichia coli*. *Proc Natl Acad Sci U S A* 104: 6043–6048

Levin D, Schneider WM, Hoffmann HH, Yarden G, Busetto AG, Manor O, Sharma N, Rice CM, Schreiber G (2014) Multifaceted activities of type I interferon are revealed by a receptor antagonist. *Sci Signal* 7: ra50

Maiwald T, Schneider A, Busch H, Sahle S, Gretz N, Weiss TS, Kummer U, Klingmüller U (2010) Combining theoretical analysis and experimental data generation reveals IRF9 as a crucial factor for accelerating interferon α-induced early antiviral signalling. *FEBS J* 277: 4741–4754

Makris S, Paulsen M, Johansson C (2017) Type I interferons as regulators of lung inflammation. *Front Immunol* 8: 259

Malakhova OA, Kim KI, Luo JK, Zou W, Kumar KG, Fuchs SY, Shuai K, Zhang DE (2006) UBP43 is a novel regulator of interferon signaling independent of its ISG15 isopeptidase activity. *EMBO J* 25: 2358–2367

Mazewski C, Perez RE, Fish EN, Platanias LC (2020) Type I interferon (IFN)-regulated activation of canonical and non-canonical signaling pathways. *Front Immunol* 11: 606456

McNab F, Mayer-Barber K, Sher A, Wack A, O'Garra A (2015) Type I interferons in infectious disease. *Nat Rev Immunol* 15: 87–103

Megger DA, Philipp J, Le-Trilling VTK, Sitek B, Trilling M (2017) Deciphering of the human interferon-regulated proteome by mass spectrometry-based quantitative analysis reveals extent and dynamics of protein induction and repression. *Front Immunol* 8: 1139

Mendoza JL, Schneider WM, Hoffmann HH, Vercauteren K, Jude KM, Xiong A, Moraga I, Horton TM, Glenn JS, de Jong YP *et al* (2017) The IFN-λ-IFN-λR1-IL-10Rβ complex reveals structural features underlying type III IFN functional plasticity. *Immunity* 46: 379–392

Mesev EV, LeDesma RA, Ploss A (2019) Decoding type I and III interferon signalling during viral infection. *Nat Microbiol* 4: 914–924

Mi H, Muruganujan A, Huang X, Ebert D, Mills C, Guo X, Thomas PD (2019) Protocol update for large-scale genome and gene function analysis with the PANTHER classification system (v.14.0). *Nat Protoc* 14: 703–721

Mitchell S, Mercado EL, Adelaja A, Ho JQ, Cheng QJ, Ghosh G, Hoffmann A (2019) An NFκB activity calculator to delineate signaling crosstalk: type I and II interferons enhance NFκB via distinct mechanisms. *Front Immunol* 10: 1425

Mitrophanov AY, Groisman EA (2008) Positive feedback in cellular control systems. *Bioessays* 30: 542–555

Mitrophanov AY, Hadley TJ, Groisman EA (2010) Positive autoregulation shapes response timing and intensity in two-component signal transduction systems. *J Mol Biol* 401: 671–680

Pervolaraki K, Stanifer ML, Münchau S, Renn LA, Albrecht D, Kurzhals S, Senís E, Grimm D, Schröder-Braunstein J, Rabin RL *et al* (2017) Type I and type III interferons display different dependency on mitogen-activated protein kinases to mount an antiviral state in the human gut. *Front Immunol* 8: 459

Pervolaraki K, Rastgou Talemi S, Albrecht D, Bormann F, Bamford C, Mendoza JL, Garcia KC, McLauchlan J, Höfer T, Stanifer ML *et al* (2018) Differential induction of interferon stimulated genes between type I and type III interferons is independent of interferon receptor abundance. *PLoS Pathog* 14: e1007420

Pfeffer LM (2011) The role of nuclear factor κB in the interferon response. *J Interferon Cytokine Res* 31: 553–559

Quinlan AR, Hall IM (2010) BEDTools: a flexible suite of utilities for comparing genomic features. *Bioinformatics* 26: 841–842

Read SA, Wijaya R, Ramezani-Moghadam M, Tay E, Schibeci S, Liddle C, Lam VWT, Yuen L, Douglas MW, Booth D *et al* (2019) Macrophage coordination of the interferon lambda immune response. *Front Immunol* 10: 2674

Reder AT, Feng X (2014) How type I interferons work in multiple sclerosis and other diseases: some unexpected mechanisms. *J Interferon Cytokine Res* 34: 589–599

Rijckborst V, Janssen HL (2010) The role of interferon in hepatitis B therapy. *Curr Hepat Rep* 9: 231–238

Sadler AJ, Williams BR (2008) Interferon-inducible antiviral effectors. *Nat Rev Immunol* 8: 559–568

Sanjana NE, Shalem O, Zhang F (2014) Improved vectors and genome-wide libraries for CRISPR screening. *Nat Methods* 11: 783–784

Schioppa T, Sozio F, Barbazza I, Scutera S, Bosisio D, Sozzani S, Del Prete A (2020) Molecular basis for CCRL2 regulation of leukocyte migration. *Front Cell Dev Biol* 8: 615031

Schneider WM, Chevillotte MD, Rice CM (2014) Interferon-stimulated genes: a complex web of host defenses. *Annu Rev Immunol* 32: 513–545

Schreiber G, Piehler J (2015) The molecular basis for functional plasticity in type I interferon signaling. *Trends Immunol* 36: 139–149

Shalem O, Sanjana NE, Hartenian E, Shi X, Scott DA, Mikkelson T, Heckl D, Ebert BL, Root DE, Doench JG *et al* (2014) Genome-scale CRISPR-Cas9 knockout screening in human cells. *Science* 343: 84–87

Staels F, Collignon T, Betrains A, Gerbaux M, Willemsen M, Humblet-Baron S, Liston A, Vanderschueren S, Schrijvers R (2021) Monogenic adult-onset inborn errors of immunity. *Front Immunol* 12: 753978

Stanifer ML, Pervolaraki K, Boulant S (2019) Differential regulation of type I and type III interferon signaling. *Int J Mol Sci* 20: 1445

Stark GR, Darnell JE Jr (2012) The JAK-STAT pathway at twenty. *Immunity* 36: 503–514

Su X, Yee LJ, Im K, Rhodes SL, Tang Y, Tong X, Howell C, Ramcharran D, Rosen HR, Taylor MW *et al* (2008) Association of single nucleotide polymorphisms in interferon signaling pathway genes and interferon-stimulated genes with the response to interferon therapy for chronic hepatitis C. *J Hepatol* 49: 184–191

Sugrue JA, Bourke NM, O'Farrelly C (2021) Type I interferon and the Spectrum of susceptibility to viral infection and autoimmune disease: a shared genomic signature. *Front Immunol* 12: 757249

Tangye SG, Al-Herz W, Bousfiha A, Chatila T, Cunningham-Rundles C, Etzioni A, Franco JL, Holland SM, Klein C, Morio T *et al* (2020) Human inborn errors of immunity: 2019 update on the classification from the International Union of Immunological Societies Expert Committee. *J Clin Immunol* 40: 24–64

Tong AJ, Liu X, Thomas BJ, Lissner MM, Baker MR, Senagolage MD, Allred AL, Barish GD, Smale ST (2016) A stringent systems approach uncovers gene-specific mechanisms regulating inflammation. *Cell* 165: 165–179

Trilling M, Bellora N, Rutkowski AJ, de Graaf M, Dickinson P, Robertson K, Prazeres da Costa O, Ghazal P, Friedel CC, Albà MM *et al* (2013) Deciphering the modulation of gene expression by type I and II interferons combining 4sU-tagging, translational arrest and in silico promoter analysis. *Nucleic Acids Res* 41: 8107–8125

Wadman M (2020) Flawed interferon response spurs severe illness. *Science* 369: 1550–1551

Wang N, Lefaudeux D, Mazumder A, Li JJ, Hoffmann A (2021) Identifying the combinatorial control of signal-dependent transcription factors. *PLoS Comput Biol* 17: e1009095

de Weerd NA, Nguyen T (2012) The interferons and their receptors—distribution and regulation. *Immunol Cell Biol* 90: 483–491

Werner SL, Barken D, Hoffmann A (2005) Stimulus specificity of gene expression programs determined by temporal control of IKK activity. *Science* 309: 1857–1861

Xiong W, Ferrell JE Jr (2003) A positive-feedback-based bistable 'memory module' that governs a cell fate decision. *Nature* 426: 460–465

Ye L, Schnepf D, Staeheli P (2019) Interferon-λ orchestrates innate and adaptive mucosal immune responses. *Nat Rev Immunol* 19: 614–625

Yen M, Ren J, Liu Q, Glassman CR, Sheahan TP, Picton LK, Moreira FR, Rustagi A, Jude KM, Zhao X *et al* (2022) Facile discovery of surrogate cytokine agonists. *Cell* 185: 1414–1430.e19

Zhang Y, Liu T, Meyer CA, Eeckhoute J, Johnson DS, Bernstein BE, Nusbaum C, Myers RM, Brown M, Li W *et al* (2008) Model-based analysis of ChIP-seq (MACS). *Genome Biol* 9: R137

Zhang Q, Bastard P, Liu Z, Le Pen J, Moncada-Velez M, Chen J, Ogishi M, Sabli IKD, Hodeib S, Korol C *et al* (2020) Inborn errors of type I IFN immunity in patients with life-threatening COVID-19. *Science* 370: eabd4570

# Expanded View Figures
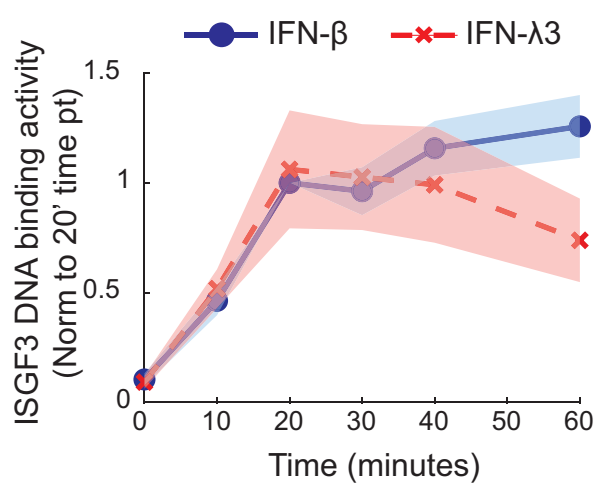


**Figure EV1.  IFN-β and IFN-λ3 show comparable ISGF3 activation at the selected concentrations.**

Quantified ISGF3 activity upon IFN-β (10 U/ml, blue) and IFN-λ3 (100 ng/ml, red) stimulation measured by an electrophoretic mobility shift assay (EMSA). Data are a subset of the time course data from Fig 2 indicating the ISGF3 activity in the first hour (i.e., activation phase).

Source data are available online for this figure.

**Figure EV2.  Applying the adapted IFN signaling dynamical network model to assess STAT2- and IRF9-feedback loop-dependent temporal signaling dynamics.**

Using the adapted IFN signaling model (Fig 3), simulations predict ISGF3 binding activity, nuclear and cytoplasmic active and total protein species, and mRNA species when positive feedback loops for STAT2 (yellow line), IRF9 (purple line), and STAT1 (green line) are eliminated or not (thick blue line) during IFN-β stimulation.
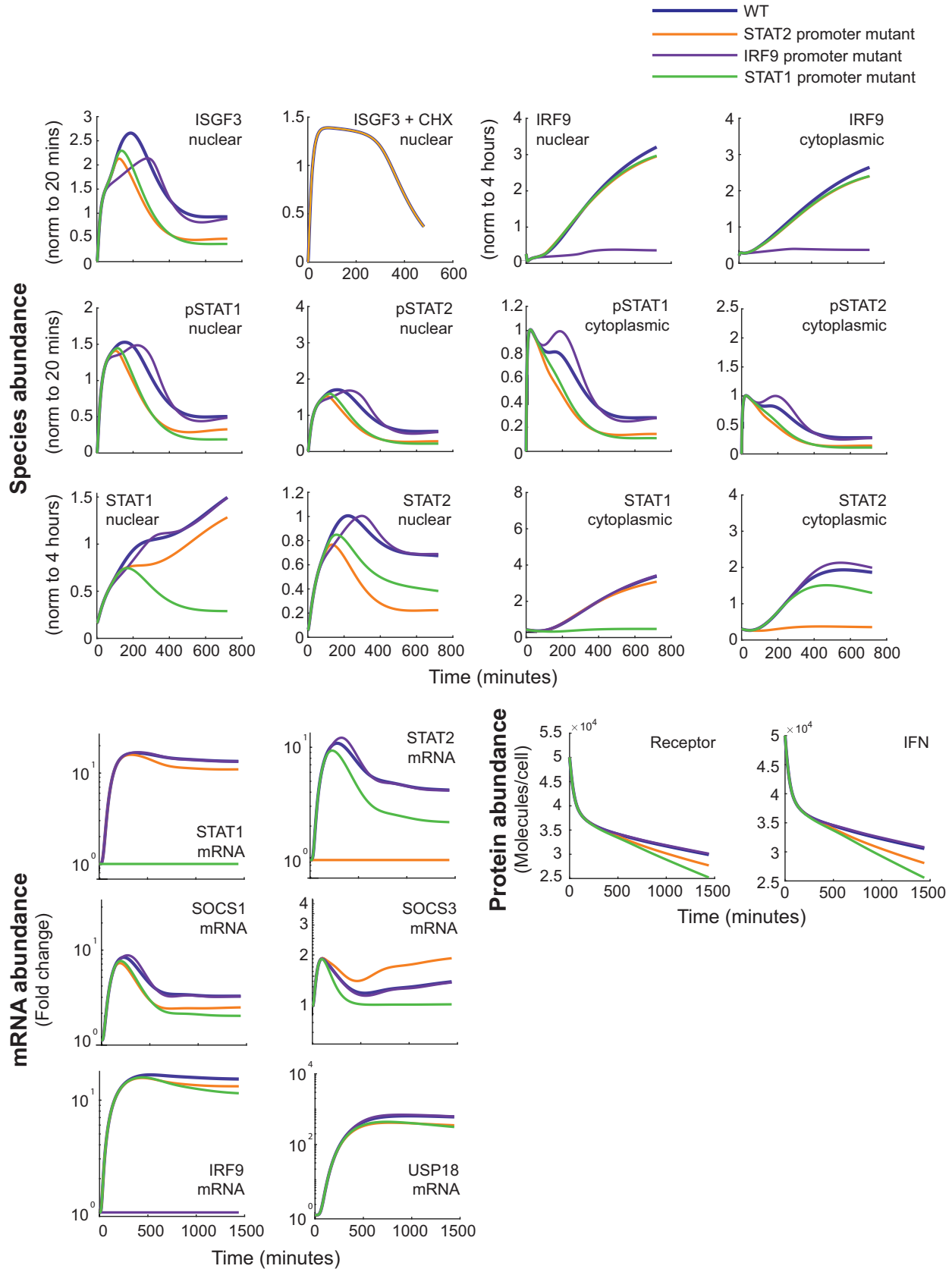
**Figure EV2.**

**Figure EV3.   CRISPR-Cas9 gene editing effectively mutates ISGF3 binding motifs in STAT2 and IRF9 gene promoters.**

A   Nucleotide sequences of the promoter regions of murine IRF9 (ENSMUSG00000002325) and STAT2 (ENSMUSG00000040033) genes containing an ISGF3 binding motif. Distance from TSS was selected based on the locus of the IRF9 transcript (ENSMUST00000138037.2) and STAT2 transcript (ENSMUST00000085708.3). Data of the IRF9 promoter and STAT2 promoter regions from cDNA of IRF9 promoter and STAT2 promoter mutant MLE-12 lung epithelial cells measured using Sanger sequencing. Alterations near the targeted ISGF3 binding motif are indicated in red text. Data are from two biological replicates.

B   Pie charts of unique DNA sequences of the promoter regions of IRF9 and STAT2 genes, indicating the percentage of DNA sequences of the promoter region of IRF9 and STAT2 from IRF9 promoter and STAT2 promoter mutant cells, respectively, measured using amplicon sequencing. The WT variant compromised 21% of the total IRF9 DNA and 9% of the STAT2 DNA, with mutant variants found in the remaining 79 and 91%, respectively.

Source data are available online for this figure.

**A**

| | | |
|---|---|---|
| Distance from TSS | -467 | ISGF3 binding | -435 |
| IRF9 promoter | AGACCACGTGGTTTCT***AGG***AAATGCACCTCCCC |
| IRF9 promoter mutant rep1 | NGACNAC - - - - - - - - -GTG**NNN**TNCNCCTCCCC |
| IRF9 promoter mutant rep2 | NGACNNCGTGGTTTCT**NNGANNNN**CNCCNCCCC |

| | | |
|---|---|---|
| Distance from TSS | -314 | ISGF3 binding | -276 |
| STAT2 promoter | TTCACGCAC***CCT***GGTTTCAGTTTCCTTTCCCTAGAACTC |
| STAT2 promoter mutant rep1 | TTC -CGCN**CCC**TGGTT**NNTTTNCNTTN**CCNNAAANCCCN |
| STAT2 promoter mutant rep2 | TTC -CGCACCCTGGTTC - -N**TTTCTTTT**CCCAANANNNN |

**B**

### Percentage of IRF9 promoter sequences
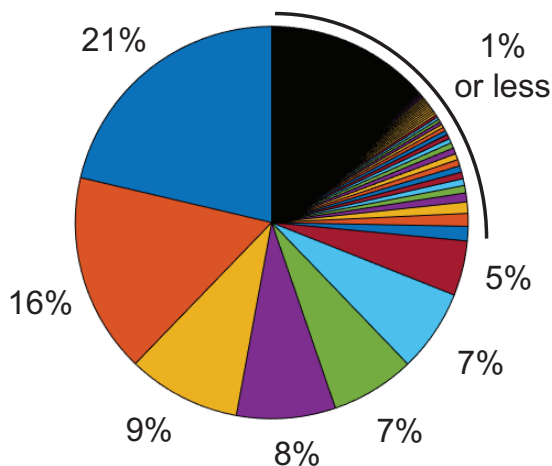


| % | Sequence |
|---|---|
| 21 | AGACCACGTGGTTTCTAGGAAATGCACCTCCCC |
| 16 | TGACACAGAGGATGGGGTT |
| 9 | AGACCACGTGGTCTAGGAAATGCACCTCCCC |
| 8 | AGACCACGTGGAAATGCACCTCCCC |
| 7 | GCCCATGTGTCAGAAAAGAAGGGACTCTCAAGCCCC |
| 7 | AGACTCATGGCCACCCTCT |
| 5 | AGACCACGTGGTTCTAGGAAATGCACCTCCCC |

### Percentage of STAT2 promoter sequences
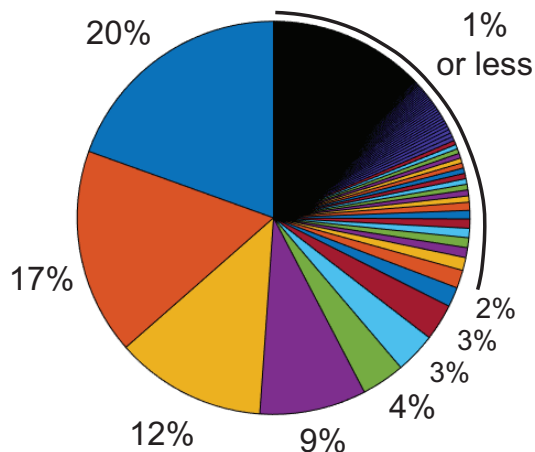


| % | Sequence |
|---|---|
| 20 | TTCACGCACCCTGGTTCAGTTTCCTTTCCCTAGAACTC |
| 17 | TTCACGCACCCTGTTCAGTTTCCTTTCCCTAGAACTC |
| 12 | TTCACGCACCCTGGTTTCAGTTTCCTTTCCCTAGAACTC |
| 9 | TTCACGCACCCTGGTTTCAGTTTCCTTTCCCTAGAACTC |
| 4 | TTCACGCACCCTGGTCAGTTTCCTTTCCCTAGAACTC |
| 3 | TTCACGCACCCTGGTTTCCTTTCCCTAGAACTC |
| 3 | TTCACGCACCCTTCAGTTTCCTTTCCCTAGAACTC |

**Figure EV3.**